THESIS

PROCESSES DRIVING SHALLOW CONVECTIVE DEVELOPMENT AND THEIR INTERACTIONS WITH AEROSOLS: AEROSOL TRANSPORT AND AEROSOL BREEZES

Submitted by

Gabrielle R. Leung

Department of Atmospheric Science

In partial fulfillment of the requirements

For the Degree of Master of Science

Colorado State University

Fort Collins, Colorado

Fall 2022

Master's Committee:

Advisor: Susan C. van den Heever

Sonia M. Kreidenweis
Shantanu Jathar

ABSTRACT

PROCESSES DRIVING SHALLOW CONVECTIVE DEVELOPMENT AND THEIR INTERACTIONS WITH AEROSOLS: AEROSOL TRANSPORT AND AEROSOL BREEZES

In this two-part thesis we investigate the development of tropical shallow convective clouds (i.e. shallow cumulus and cumulus congestus) and their interactions with the aerosol environment using idealized large-eddy simulations (LES). Although much about shallow convection is well-understood, we specifically focus on three facets of shallow convection that remain understudied: (1) the factors governing the development of congestus extending above the 0ºC stable layer; (2) the detrainment of aerosol particles and water vapor from congestus clouds into the mid-troposphere; and (3) the impacts of strong horizontal gradients in aerosol concentration on mesoscale circulations.

Part one of this study explores environmental controls on congestus development and the implications of that development on aerosol lofting and transport. Congestus is the middle mode of tropical convection, with cloud tops around or exceeding the 0ºC level (~5km AGL). While some congestus are *terminal*, meaning capped by the 0ºC stable layer, others are *transient* and may develop into deep convection. Although this distinction impacts the congestus-to-deep convection transition and the convective transport of water vapor and aerosols into the mid-troposphere, there is still much to be understood about the processes causing congestus to overshoot the 0℃ level and continue growing. We find that terminal and transient congestus updrafts are characterized by a similar overturning circulation between the updraft and subsiding shell. However, transient congestus have stronger updrafts, and importantly, the downward

branch of their corresponding circulations is constrained by the 0ºC level. Our findings support previous results suggesting buoyancy as a control on congestus height, and we specifically demonstrate that congestus developing in more humid midlevel environments are more likely to be transient. We additionally determine that terminal congestus regenerate more aerosol via evaporation along their cloud edges, while transient congestus create stronger midlevel detrainment layers of aerosol and water vapor due to the trapping of the regenerated aerosol above the 0ºC level. Such midlevel detrainment layers are important for the formation of altocumulus clouds.

Part two of this study introduces and explores the concept of an "aerosol breeze", a thermally-driven circulation resulting from mesoscale gradients in aerosol loadings. We call the resulting circulation an aerosol breeze so as to be analogous to well-documented circulations associated with heterogenous surfaces, like sea breezes. The aerosol-induced circulation sets up a gradient in convection and precipitation that is opposite in direction to that of the aerosol gradient. Clouds in the presence of an aerosol gradient precipitate sooner and more intensely than those in the same integrated aerosol loading distributed horizontally homogeneously. These results suggest unrepresented sub-grid scale heterogeneity in aerosol emissions may lead to biases in simulated cloudiness and precipitation. We also present two observational case studies of aerosol breezes that are similar to our model results in scale and cloud distribution. Further study of the aerosol breeze phenomena is warranted, especially in regions where strong aerosol gradients may be expected, such as along the edges of wildfire plumes or urbanized regions.

ACKNOWLEDGEMENTS

Science is never done in isolation—not even when socially distancing during a global pandemic—and so I want to acknowledge the (sometimes invisible) contributions of the people who make my work possible.

First, I am grateful to my advisor and co-author, Dr. Susan C. van den Heever. Sue gave me a chance even before I had ever run a model, or even knew what a "cloud process" really was. Every day since, she has pushed me to be a better scientist, to believe in my own work, and to keep challenging myself.

I want to thank Dr. Sonia Kreidenweis and Dr. Shantanu Jathar, for their time, perspective, and generosity in serving as my committee members.

This work wouldn't have been possible without the rest of the van den Heever group, past and present: Steve Saleeby, Dr. Leah Grant, Dr. Emily Riley Dellaripa, Dr. Bowen Pan, Dr. Sean Freeman, Dr. Alex Sokolowsky, Nick Falk, Ben Ascher, Christine Neumaier, Dr. Jennie Bukowski, Dr. Minnie Park, Dr. Yasutaka Murakami, Kristen van Valkenburg, Dr. Peter Marinescu, Dr. Rick Schulte, Dr. Ross Heikes, Dr. Brenda Dolan, Katy Burger. Thank you for sharing your ideas (science and otherwise), programming tips, inside jokes, and snacks.

I want to thank the CSU Department of Atmospheric Science staff for their help—in particular, Amanda Davey and Sarah Tisdale have always been incredibly thoughtful and patient.

I've been lucky enough to have participated in the NASA Cloud, Aerosol, and Monsoon Processes Philippines Experiment ($CAMP^2Ex$) and the NSF BioAerosols and Convective Storms (BACS) field campaigns. I especially want to thank Leah Grant for leading the BACS campaign to such success, Sean Freeman for teaching me how to fly drones (and not being upset when we

unilaterally reorganized the drone lab), and the BACS drone team—Allie Mazurek, Jacob Escobedo, Daniel Veloso Águila, Nick Falk, Ben Ascher, Christine Neumaier, Brian Heffernan, and Marina Nieto —for being such great company on long and tiring deployment days.

The Atmospheric Science International Students and Scholars Association (ATSISSA)—especially my co-board members Wei-Ting Hsiao and Zaibeth Carlo Frontera—make navigating a foreign country a lot less lonely through potlucks and board game nights.

My undergraduate mentors, Dr. Obie Cambaliza and Dr. Gemma Narisma**,** have opened so many doors in my life, and always made sure I had every opportunity that I wanted and was willing to work for.

I'm also incredible fortunate to have friends who rooting for me no matter the distance: Martina, Oey, Ninna, Coco, Robbie, Dainie, Zel, Annelle, and Josh. I'm also thankful to Genie and Leif, who have been wonderful friends and a home away from home. Sean, Minnie, Jennie, Alex, and Matt have also been great company and have always been so welcoming to me.

I've been supported all my life by my incredible family. My brothers—Mao, Toby, and Tommy—never fail to send me ridiculous pictures of our dogs when I miss them. And I am so thankful to my dad—JP—and grandparents—Tami, Nelson, and Nita—who supported me even when I decided to move 14 (sometimes 15) time zones away from them. Of course, I am grateful to my partner Miguel Hilario: thank you for always being willing to talk science (or sometimes, to talk about anything except science), for killing time with me in various airports and quarantine hotels, and for generally just being the best support system I could have asked for.

Finally, the work in this thesis has been supported through NASA CAMP^{2}Ex grant #80NSSC18K0149. Computing resources were provided by the NASA High-End Computing (HEC) Program at the Ames Research Center.

TABLE OF CONTENTS

CHAPTER 1: INTRODUCTION

1.1 Background and motivation

Many of the factors controlling the formation, development, and organization of tropical shallow convective clouds (i.e. shallow cumulus and cumulus congestus) have been well-studied and well-understood since the 1950's (Malkus 1952; Cotton et al. 2011; Randall et al. 2019). The typical conceptual model of a cumulus cloud is one of a plume or chain of thermals originating in boundary layer eddies (Scorer and Ludlam 1953; Heus et al. 2009; Hernandez-Deckers and Sherwood 2016; Moser and Lasher-Trapp 2017; Morrison et al. 2020). These clouds then ascend, and either grow, or decay, depending on their dynamical and microphysical interactions with environmental parameters such as static stability, tropospheric moisture, and even aerosol concentrations.

Climatological stable layers in the tropics (e.g. trade wind inversions, 0ºC stable layer) are known to be important for constraining the vertical development of shallow cumulus and congestus clouds (Johnson et al. 1999; Posselt et al. 2008). It is also generally agreed that turbulent mixing and the entrainment of environmental air is crucial for describing convective development (Siebesma 1998; de Rooy et al. 2013), though there is some disagreement regarding the origin and properties of air actually entrained into updrafts (Heus and Jonker 2008; Schmeissner et al. 2015; Smalley and Rapp 2020; Drueke et al. 2020), and the parameterization of entrainment continues to be a source of uncertainty in large-scale models (Rougier et al. 2009). In more recent years, the impacts of aerosol particles on warm-phase convection have received much attention, both in terms of their direct radiative and indirect microphysical effects (Jiang and Feingold 2006; Tao et al. 2012; Sheffield et al. 2015; Igel and van den Heever 2021).

A substantial body of research exists on the processes driving the development of shallow clouds, not only because they are ubiquitous and relatively simple cloud systems—at least relative to cumulonimbus, severe convective storms, or mesoscale convective systems—but also because they play numerous important roles within the climate system as a whole. Shallow convective clouds control the tropical mass and energy flux budgets by mixing typically dry and relatively-clean free-tropospheric air into the boundary layer and vice-versa through convective transport and detrainment (Kuang and Bretherton 2006; Stevens 2007; Takayabu et al. 2010). In doing so, they are important contributors to the global circulation (Riehl and Malkus 1958). Furthermore, because they represent a significant amount of tropical cloud cover and rainfall (Jensen and Del Genio 2006; van den Heever et al. 2011), the radiative feedbacks from shallow clouds are important for organizing/aggregating convection (Waite and Khouider 2010; Muller and Held 2012; Naumann et al. 2017). The response of marine boundary layer clouds to climate change has also been shown to be a key source of uncertainty in global climate models (GCMs) (Bony and Dufresne 2005; Medeiros et al. 2015). Finally, because their updrafts tend to be relatively weaker than updrafts in deeper convection, shallow clouds such as cumulus and congestus tend to be more sensitive to environmental perturbations such as changes to the aerosol loading (Li et al. 2013a; Sheffield et al. 2015; Igel and van den Heever 2021) and surface fluxes (Gentine et al. 2019).

Despite the breadth of research on and the clear significance of shallow clouds, there continue to be facets of their development that are not fully understood. Often, we are able to address these gaps in knowledge based on well-placed observations obtained during intensive field campaigns, which are extremely valuable for advancing our scientific understanding. However, observations only inform us about the state of a system and cannot be used to directly

assess cloud processes. Numerical modeling facilitates our capabilities to understand the mechanisms and physical processes that drive those observed phenomena. Idealized simulations in particular can help in boiling down complicated snapshots of "cloud scenes" into more straightforward and testable science questions.

The two studies that comprise this thesis both attempt to answer questions originating from the observations made during the Clouds, Aerosol, and Monsoon Processes Philippines Experiment (CAMP^{2}Ex) campaign conducted in the summer of 2019 (Reid et al. 2022). CAMP^{2}Ex made extensive and varied measurements of tropical convection, with a particular focus on the interactions between the large-scale environment, aerosol particles, and shallow tropical convective clouds. In particular, the studies here focus on three separate but interrelated areas of uncertainty observed during CAMP2Ex: (1) the factors governing the variability in congestus development; (2) the processes allowing for transport of aerosol particles into the mid-troposphere; and (3) the impacts of strong horizontal gradients in aerosol concentration on mesoscale circulations. The work herein uses high-resolution large eddy simulations (LES) to explain the dynamical and microphysical mechanisms driving variability in shallow convective development and the interactions between shallow clouds and the aerosol environment, as was observed during CAMP^{2}Ex—however, by virtue of using an idealized modelling framework, our work is also able to shed light on the fundamental physical processes controlling shallow tropical convection and governing its interactions with the aerosol environment more generally.

1.2 Thesis Outline and objectives

In Chapter 2, we examine the interactions between tropical congestus clouds and their near-environments. Whether or not a congestus cloud can overshoot the 0ºC stable layer is crucial for the congestus-to-deep convective transition (Johnson et al. 1999; Mapes et al. 2006;

Waite and Khouider 2010; Sokolowsky et al., 2022). However, the processes which determine congestus development and how those processes are influenced by the environment are still not well understood. Understanding congestus development is additionally important due to their role in the convective transport of water vapor and aerosols into the mid-troposphere (Kuang and Bretherton 2006; Takayabu et al. 2010; Dawe and Austin 2011; Reid et al. 2019). The eventual fate of the air that is transported vertically through congestus clouds has significant implications for cloud-processing of aerosol particles, the formation of altocumulous clouds, and the radiative budget overall. The first and second goals of this thesis are therefore to:

(1) Identify the environmental controls and physical processes that differentiate congestus which are capped by the 0ºC stable layer (i.e. terminal) from those which to develop past the 0ºC stable layer (i.e. transient).

(2) Characterize the differences in the detrainment of water vapor and aerosols from terminal versus transient congestus.

Thus, in Chapter 2, we first explore the structure of congestus updrafts and describe their interactions with their near-environments in order to assess the environmental factors that control their development beyond the 0ºC stable layer. We then characterize the processes involved in congestus detraining aerosol and water vapor into the midlevels, and quantify the differences in their detrainment based on their height relative to the 0ºC stable layer.

In Chapter 3, we switch our focus from the impacts of shallow convective clouds on the aerosol environment, to the impacts of the aerosol environment on shallow clouds. More specifically, we investigate the impacts of mesoscale heterogeneity in horizontal aerosol concentrations on the development of shallow convective clouds. The spatial distribution of aerosol concentrations is known to have important feedbacks on the distribution and magnitude

of clouds and precipitation, both on a global (Allen et al. 2015; Haywood et al. 2013) and regional (Herbert et al. 2021; Hodzic and Duvel 2018; Kim et al. 2016; Lau et al. 2008) scale. Although mesoscale variability in aerosol concentrations has frequently been observed, such as along the edges of wildfire smoke plumes (Kelleher et al. 2018; Palm et al. 2021) or urban areas (Lin et al. 2021; Pierce et al. 2019), it is as yet unknown as to whether this variability impacts convection. In this part of the study, we introduce the concept of an "aerosol breeze", a thermally-direct circulation driven by mesoscale gradients in aerosol concentrations—named to be analogous to other well-observed mesoscale phenomena such as sea breezes or forest breezes, which are driven by gradients in surface properties. The third goal of this thesis is to:

(3) Determine whether mesoscale horizontal gradients in aerosol loading can drive "aerosol breezes" that subsequently impact clouds and precipitation.

Finally, in Chapter 4, we present a summary of the major findings and implications of this thesis research.

CHAPTER 2: CONTROLS ON THE DEVELOPMENT AND CIRCULATION OF TERMINAL VERSUS TRANSIENT CONGESTUS CLOUDS AND IMPLICATIONS FOR MIDLEVEL AEROSOL TRANSPORT[1]

2.1 Introduction

The three modes of tropical convection—shallow cumulus, cumulus congestus, and deep convection—are capped by layers of increased static stability at the trade wind inversion (~2km AGL), the 0℃ stable layer (~5km AGL), and the tropopause (~15-16 km AGL), respectively (Johnson et al. 1999; Masunaga et al. 2005; Posselt et al. 2008). The congestus mode is relatively understudied compared to shallow cumulus and deep convection, but is still of interest due to its role as an intermediary in the transition from shallow to deep convection (Mapes et al. 2006; Waite and Khouider 2010), its capacity to flux mass and energy into the midlevels (Kuang and Bretherton 2006; Takayabu et al. 2010), and its significant contribution to tropical precipitation (Lau and Wu 2003; Jensen and Del Genio 2006; van den Heever et al. 2011). Furthermore, because their updrafts are somewhat weaker than deep convective clouds, congestus are also more susceptible to aerosol forcing than faster and deeper updrafts since the resulting warm-phase invigoration is not offset by changes to ice-phase microphysics as in deep convection (Li et al. 2013a; Sheffield et al. 2015). Understanding the factors that govern congestus development and their potential transition into deep convection is therefore important for improving scientific understanding and model representation of tropical convection.

[1] This study, titled "Controls on the Development and Circulation of Terminal versus Transient Congestus Clouds and Implications for Midlevel Aerosol Transport" (Leung, G.R. and S.C. van den Heever, 2022) has been accepted in the Journal of the Atmospheric Sciences.

Within the congestus mode it is important to distinguish between what are referred to as terminal and transient congestus (Luo et al. 2009) in order to enhance our understanding of both convective detrainment and the shallow to deep convection transition. In Johnson et al. (1999), congestus are identified in relation to the 0ºC stable layer, but they also found considerable numbers of congestus overshooting this level. Luo et al. (2009) defined terminal congestus as those which have ceased to develop vertically past this 0ºC stable layer (~4-6km AGL). Terminal congestus typically detrain around that stable layer, which is formed from the melting of hydrometeors from dissipating anvil clouds and other mixed-phase clouds (Johnson et al. 1999) and sustained by clear air subsidence and radiative cooling (Posselt et al. 2008). On the other hand, transient congestus penetrate this stable layer and continue developing aloft. These transient congestus may later become deep convective clouds if the additional latent heat released in the mixed-phase regions above the 0℃ level sufficiently increases the updraft buoyancy (Johnson et al. 1999; Li et al. 2013a; Sheffield et al. 2015; Mecikalski et al. 2016). The development of congestus above the 0℃ level, and subsequent latent heat release in mixed-phase regions, has implications for the flux of energy and moisture into the midlevels and beyond, since ice processes are crucial to the mechanisms by which tropical convection drives large-scale circulations such as the Hadley cell (Riehl and Malkus 1958; Zipser 2003; Fierro et al. 2009; McGee and van den Heever 2014). The proportion of congestus clouds that are transient may also impact the vertical transport of boundary layer air, water vapor, energy and aerosols, into the mid- and upper levels of the troposphere (Dawe and Austin 2011; Reid et al. 2019), from where they may subsequently influence other cloud processes including new cloud formation.

Traditionally, the differences in development between terminal and transient congestus have been attributed to buoyancy, which has been used in remote sensing studies to identify

which congestus are likely to continue developing (Luo et al. 2009). It is thought that terminal congestus either have less low-level environmental convective available potential energy (CAPE) to begin with; are limited by the entrainment of dry air above the boundary layer, which leads to evaporation of droplets and a subsequent reduction in buoyancy; or are unable to regain positive buoyancy upon encountering the 0℃ stable layer (Redelsperger et al. 2002). There is some observational and modeling evidence to support the dominant role of dry air entrainment in governing congestus buoyancy and overall height, showing that the cloud top height (CTH) distribution is more strongly correlated with midlevel humidity than low-level CAPE or the magnitude of midlevel stability (Redelsperger et al. 2002; Takemi et al. 2004; Jensen and Del Genio 2006). However, the prior focus on correlations between environmental parameters and the population CTH distribution have not included establishing the mechanisms by which the environment influences the development of individual congestus clouds or ensembles of congestus. Momentum budgets have been analyzed for thermals and deep convective clouds. In general, these studies agree that the primary forces acting on thermals and on steady-state cloud ensembles are buoyancy and perturbation pressure gradient forces (PPGF), with lesser contributions from momentum entrainment (de Roode et al. 2012; Sherwood et al. 2013; Romps and Charn 2015; Peters 2016; Morrison and Peters 2018; Tian et al. 2019), although the relative magnitudes of each force depend on whether the full cloud volume or only the updraft volume is being considered (Wang and Zhang 2014; Savre 2021). While such momentum budgets have been analyzed for thermals and deep convection, similar momentum budget analysis has not been conducted specifically for congestus clouds. A more detailed analysis of congestus updraft momentum budgets would therefore be valuable, especially for potential applications to cumulus parameterizations. The physical mechanisms that govern whether a congestus cloud becomes

transient or remains terminal—in particular, whether this can be determined by buoyancy alone—are still not yet well understood. Determining controls on congestus cloud top height will help to improve model representations of convective development processes, cloud top height distributions, as well as the overall energy and moisture budgets, and will allow us to assess how these may change in a warming climate. A better understanding of congestus acceleration budgets would also aid in understanding the physical processes behind aerosol impacts on congestus and how these are represented in models (Sheffield et al. 2015; Marinescu et al. 2021), though specific work on aerosol impacts on congestus is left for a future study.

In this work, we attempt to better characterize the dynamical and microphysical processes governing congestus development. Particular focus is given to identifying those factors which differentiate transient and terminal congestus, and how those differences impact the detrainment of water vapor and aerosols from congestus into the midlevels. Specifically, this study aims to answer two questions: (1) What physical mechanisms allow transient congestus to overshoot the 0℃ level and continue developing while terminal congestus are capped? and (2) How does congestus cloud top height relative to the 0℃ level impact the detrainment of water vapor and aerosols? An idealized, high-resolution large eddy simulation (LES) of a tropical congestus field provides a robust sample of congestus updrafts to identify, composite, and analyze. Differences between transient and terminal composites are explored in terms of updraft and near-environment structure, as well as the physical processes governing those distributions. Finally, the differences in the circulations of terminal and transient congestus are explored in terms of their implications for convective transport of aerosol particles, specifically in terms of their impact on midlevel detrainment of aerosol and water vapor.

2.2 Model description and analysis approach

a Model description

We perform the simulations for this study with the Regional Atmospheric Modeling System (RAMS) (Cotton et al. 2003; Saleeby and van den Heever 2013), a non-hydrostatic cloud-resolving model with advanced microphysics and aerosol schemes. RAMS uses a two-moment, bin-emulating bulk microphysics scheme. Cloud water, rainwater, and five ice hydrometeor species (pristine ice, snow, aggregates, graupel, and hail) were enabled to capture both the warm and mixed-phase processes found in congestus clouds. Cloud droplets are activated from available cloud condensation nuclei (CCN) when sufficient water supersaturation is achieved. In the mixed-phase, cloud water can be transferred to ice species by contact nucleation, riming, the Wegner-Bergeron-Findeisen process, and homogenous freezing (Saleeby and Cotton 2008; Saleeby and van den Heever 2013). Heterogenous nucleation via deposition nucleation, condensation freezing, and immersion freezing are parameterized for temperatures below 0ºC based on DeMott et al. (2010).

RAMS aerosol mass budget capabilities were also enabled to further track the proportion of aerosol in four categories: (1) unprocessed aerosol, (2) in-hydrometeor aerosol, (3) regenerated aerosol, and (4) surface-accumulated aerosol (Saleeby and van den Heever 2013). Aerosol particles are removed from the domain upon the activation of cloud droplets, which transfers the aerosol mass to an in-cloud category and then to other in-hydrometeor categories as cloud mass is transferred between liquid and ice hydrometeors. Hydrometeor evaporation under subsaturated conditions transfers the in-hydrometeor aerosol mass to a regenerated aerosol category. Those aerosols that are not activated remain in the unprocessed aerosol category. The amount of aerosol accumulated onto the surface via wet deposition or rainout is also tracked.

Aerosol particles can be advected around the domain and a negligible proportion of the initial aerosol mass is lost to diffusion and dry deposition. Additional details about the representation of aerosol processes are available in Saleeby and van den Heever (2013).

b Model configuration and initialization

The idealized simulations were run over a fully oceanic domain with a fixed sea surface temperature and doubly periodic lateral boundaries. The domain was 100km x 100km in the horizontal with a grid spacing of 100m. The vertical grid consisted of 120 levels spanning ~15km, with grid spacing stretching from 50 to 200m. There are 18 model levels between the surface and 1km, and 63 model levels between the surface and the 0℃ level (~5.1km). The simulation was run for 48 hours from 0 UTC (8 a.m. local time), with a timestep of 0.75s and output files produced every 5 minutes. This high spatiotemporal resolution allows the model to resolve large turbulent eddies and capture the detailed horizontal and vertical structure of congestus updrafts, subsiding shells, and detrainment layers (Peters et al. 2019; Savre 2021) . Surface fluxes of heat and moisture are prognosed using the LEAF-3 submodel (Walko et al. 2000).

Initial conditions were horizontally homogenous and based on a dropsonde from the Cloud, Aerosol, and Monsoon Processes Philippines Experiment ($CAMP^2Ex$) (Reid et al. 2021). This dropsonde was selected because it sampled the tropical maritime environment near several congestus clouds, and because it allowed a congestus field to develop for several hours before transitioning towards deeper convective modes. The dropsonde was taken at approximately 3UTC, close to the initialization time of the model. The dropsonde profile was vertically smoothed by taking the mean value every 150m to reduce sudden discontinuities in the data while maintaining the observed stable layers. To represent atmospheric information above the

dropsonde launch altitude, ERA-5 data from the same time period were averaged over a 1ºx1º box containing the congestus field (between 8-9ºN, 119-120ºE). A weighted average of the dropsonde and ERA-5 profiles was taken between 5 and 6km AGL, such that the resulting profile tapered off linearly between the dropsonde profile at 5km AGL to the ERA-5 profile at 6km AGL. The resulting smoothed sounding, representing conditions favorable to the development of congestus over the ocean in the Maritime Continent (Reid et al. 2022), is shown in **Figure 2.1.** Additional observational context of congestus clouds from CAMP^{2}Ex that are similar to the clouds simulated in this paper can be found in Reid et al. (2022). It should be noted that there is vertical wind shear between 550 and 450hPa, which has been found to promote the formation of congestus over deep convection (Tian et al. 2021). Random thermal perturbations with a maximum amplitude of 0.1K were introduced within 500m AGL of the lowest model level above the surface to initiate convection.

Sulfate aerosol particles were initialized horizontally homogenously and decrease exponentially with height starting from a maximum number concentration of 500/mg at the surface, with an e-folding height of 7km. Ice nuclei were initialized with the same distribution but starting from a maximum number concentration of 0.01/mg. The size distribution of sulfate aerosol particles was represented as a log-normal with a median radius of 0.09 microns and a geometric standard deviation of 1.8, both of which are representative of the aerosol distributions measured in CAMP^{2}Ex (Reid et al. 2022). Aerosol-radiation and microphysical-radiation interactions were included in the simulation. After initialization, the model is allowed to evolve freely with no additional large-scale forcing applied. The diurnal cycle of radiation is represented using the Harrington two-stream radiation scheme, updated every 5 minutes (Harrington 1997).

The longitudinal variation of shortwave radiation is also represented (Saleeby and van den Heever 2013). Further details about the model set-up are summarized in **Table 2.1**.

c Congestus identification

Convection develops in the simulation ~5 hours after initialization. Congestus clouds develop 2.5 hours after the onset of shallow cumulus (shown by the contours in **Figure 2.2a** that reach above 4km AGL and a coincident increase in updraft velocities in **Figure 2.2b**). The first 7.5 hours of the simulation before congestus clouds develop are treated as model spin-up time and excluded from the analysis. **Figure 2.3** shows a sample of the simulated cloud field at one timestep. Although deep convection is limited in this simulation, the congestus clouds appear alongside shallower cumulus and must be separated from these other types of clouds in the simulation to facilitate the analysis. To investigate the microphysical and dynamical characteristics of the updraft core of active congestus, we only perform the analysis on cells which are cloudy (defined as having cloud liquid + ice condensate with mixing ratios greater than 0.01 g kg^{-1}) and have updrafts (defined as having vertical velocity greater than 1 m s^{-1}).

Individual congestus updrafts are identified using tobac (Tracking and Object-Based Analysis of Clouds), a recently-developed tracking algorithm that allows for the offline identification of updraft features and associated condensate volumes (Heikenfeld et al. 2019). First, two-dimensional updraft "features" are identified at each analysis timestep ($\Delta t = 5\ minutes$) using the maximum vertical velocity between 2 and 7 km in each column. For clarity, "features" are used in this paper to describe an updraft or cloudy region at one timestep, while "cells" refer to a set of updraft or cloudy features tracked as connected in time. These features are identified at multiple threshold values (1, 3, 5, and 10 m/s), and an area-weighted

centroid is assigned to each feature. Secondly, contiguous regions of cloudy grid cells are identified and, if possible, associated with a given updraft feature using a watershedding technique. A check is done to ensure that the updraft maximum is actually located within the cloudy region, and any other cloudy cells in the column that are not contiguous with the updraft maximum are excluded. From these cloudy points, the contiguous updraft region (with positive vertical velocity) is selected. Thirdly, identified updraft features are linked in time by matching up features in previous timesteps with nearby features in subsequent timesteps based on the predicted updraft motion to create trajectories of tracked "cells". Any features that are not linked to a trajectory or have a lifetime of less than 5 minutes (i.e. is not identified in at least two consecutive timesteps) are excluded from the analysis as a quality check.

Because tobac allows updrafts to be tracked in time, we can determine cloud statistics at each timestep and over the lifetime of the updraft. Cloud top height is identified for each feature as the maximum altitude where cloud condensate is greater than 0.01 g kg^{-1}, and cloud base height is similarly identified as the minimum altitude where cloud condensate reaches the threshold. For each cell trajectory, a maximum CTH is also identified from the feature CTHs at each timestep. We define congestus updrafts in this paper as cells which have (1) a cloud base at each timestep below 2km thereby excluding midlevel clouds, such as altocumulus, which have a much shallower vertical extent; (2) a maximum CTH over all timesteps between 4 and 7km; and (3) no other clouds located within the same column for at least 1km above cloud top or below cloud base at any timestep. These requirements are very similar to past studies (Sheffield et al. 2015).

It is important to note that congestus at the very beginning or very end of their life cycle, when their updrafts are weaker than 1 m s^{-1}, are excluded from the analysis. The tracking

algorithm, as with most tracking algorithms, requires a physically-informed threshold to be set as a minimum for detecting updrafts, and thus this limitation in terms of capturing the full updraft life cycle would be present for any variable used for tracking. However, due to the multiple threshold capabilities of tobac, we are able to set a fairly low minimum threshold which we believe allows us to capture a vast majority of the congestus lifetime.

d Defining terminal and transient congestus

In Luo et al. (2009), terminal and transient congestus are defined based on whether they are negatively or positively buoyant at the time of observation, and hence as to whether they will continue to vertically develop. Although we adopt the terminology *transient* and *terminal*, we use a modified definition in this paper since we are interested in whether a given congestus cloud is capped by the 0℃ stable layer.

For each tracked cell, if an identified congestus updraft belongs to a cloud with a maximum CTH between 4km and the 0ºC level (~5.1km for this simulation) throughout its tracked lifetime, it is considered *terminal*. If the maximum CTH reached over the cloud lifetime is between the 0ºC level and 7km, it is considered *transient*. Transient congestus are further subdivided at each timestep into *developing transient* and *mature transient,* based on the CTH assessed at the timestep in question. Although both developing and mature transient congestus eventually reach above the 0℃ level at some point in their lifetime, *developing transient* are those with a CTH below the 0℃ level during a given timestep, while *mature transient* are those with a CTH above it. This allows us to compare congestus before they reach the 0℃ level to see what differentiates those that are capped or constrained (i.e. terminal) from those that continue to develop vertically (i.e. developing transient). There were very few updrafts which extended

above 7km, but when identified, these were considered as deep convection and excluded from our analysis.

In this work, we track congestus and classify them as terminal or transient based on CTH at 5-minute output resolution. It is possible that a congestus may reach a greater CTH than the identified maximum CTH at some time in between sampling; in this case, this would potentially blur the classification between congestus subcategories. However, this is most likely to happen around the tallest terminal congestus (e.g. when a terminal congestus close to the 0ºC level does actually ascend above it for less than 5 minutes in between analysis times). Since the development only persists briefly, it is unlikely to significantly impact the general results.

e Compositing approach

Once congestus clouds are identified and classified as terminal or transient, they are aligned in space to generate composites of various fields for each type of congestus. This process is illustrated in **Figure 2.4**. For each congestus updraft, a given field $\psi(x, y, z)$ is redefined relative to the updraft core, defined as the centroid of updraft points at each vertical level weighted by the updraft velocity, to give a transformed field $\psi(r, \theta, z)$. Normalized coordinates are used in the radial direction, and physical coordinates are used in the vertical. The radial distance r is normalized by the updraft radius $r'(\theta, z)$, which is a function of altitude and azimuthal angle, to give $r^* = \frac{r}{r'} - 1$, such that r*<0 inside the updraft, r*=0 at the updraft edge, and r*>0 outside the updraft (**Figure 2.4a-d**).

Similar to previous analyses, an azimuthal average is taken to yield a composite field in the radial direction (Sherwood et al. 2013; Romps and Charn 2015; Peters et al. 2019; Savre 2021). The normalized composites allow for an investigation into general updraft structure without "smearing" the features by averaging updrafts of different widths. On the other hand, using

physical coordinates for the vertical dimension is useful to compare how dynamic and microphysical fields differ at fixed altitudes (e.g. the 0°C level). Such vertical composites are shown in **Figure 2.4d-f**. Key regions within the updraft referred to within the text (e.g., updraft shell, updraft core, entrainment/detrainment regions, etc.) are annotated on **Figure 2.4d-f** to assist in orientating the reader, while a more detailed description of these features can be found in Section 2.4b.

2.3 Congestus characteristics

In this section, bulk characteristics of the congestus field and differences among transient and terminal congestus are explored. A total of 1552 congestus updraft features comprising 445 tracked cells are observed (**Figure 2.5a**). The CTH distributions (**Figure 2.5b, c**) show a clear peak between 4-7km, which supports the definition of congestus clouds used in this paper. The dashed horizontal line representing the mean 0ºC level also separates the congestus distribution into two populations (terminal and transient). Terminal congestus make up 66.0% of tracked cells (**Figure 2.5a**). The other 34.0% of congestus updrafts reach above the 0°C level for at least one timestep during their tracked lifetime, with 14.0% of those extending above the 0°C level in the current timestep, and hence considered as mature transient congestus.

The proportion of transient congestus to the total number of congestus observed over the entire simulation is similar to the 30-40% of positively buoyant congestus that Luo et al. (2009) observed using CloudSat overpasses, though the definitions of terminal and transient congestus here are different than those in Luo et al. (2009). That being said, the fraction of congestus considered transient does vary over the course of the simulation.

Despite there being a greater number of terminal congestus updrafts over the simulation period (**Figure 2.5a**), transient congestus updrafts occupy a similar volume overall to the

terminal congestus updrafts (**Figure 2.5d**). In terms of mean updraft size, **Figure 2.6b** indicates that the mature transient congestus are the largest at all vertical levels. For congestus below the 0ºC level, terminal and developing transient updrafts having have similar radii below 2km, but developing transient congestus (light blue lines in **Figure 2.6b**) begin to have wider updrafts above 3km. That being said, because there are more numerous terminal congestus, they occupy a larger total area for vertical levels below 3km **(Figure 2.6a).** Although developing transient and terminal congestus updrafts have similar cloud top heights, those that will grow above the 0°C level (i.e. developing transient) tend to be wider close to the cloud top.

The overall structure of congestus updraft velocities is fairly consistent (**Figure 2.7)**. The fluctuations in updraft velocity coincide with stable layers in the domain **(Figure 2.1**): updrafts slow down as they ascend through the trade wind stable layer between 2-3km and then again at the 0°C level stable layer between 4-5.1km (dashed gray line in **Figure 2.7**). Differences between terminal and developing transient congestus updrafts become clear above 2.7km (solid gray line in **Figure 2.7**), with developing transient congestus updraft velocities being stronger thereby allowing them to ascend through the 0°C stable layer. Transient congestus continue to have faster updraft velocities until reaching maturity (**Figure 2.7e).** This increased updraft velocity enhances the ability of transient congestus to reach higher altitudes, impact the midlevel environment around the 0°C level, and thus potentially support the transition into deep convection.

2.4 Vertical acceleration budget

a Vertical acceleration calculation

In the next few sections, we investigate the physical processes driving the differences in terminal and transient congestus based on the vertical acceleration budgets. The conditionally

sampled vertical momentum equation can be written in the following form, and is similar to de Roode et al. (2012) and many cumulus parameterizations:

$$\underbrace{\frac{\partial w_c}{\partial t}}_{time\ tendency} = \underbrace{\mathrm{B}_c}_{(1)\ buoyancy} + \underbrace{-\frac{1}{\lfloor\rho\rfloor_c}\left\lfloor\frac{\partial p'}{\partial z}\right\rfloor_c}_{(2)\ perturbation\ pressure\ gradient}$$

$$+ \underbrace{-\frac{1}{A_c\lfloor\rho\rfloor_c}\oint_c \overrightarrow{v_H}\cdot\hat{n}(w-w_c)\rho dC}_{(3)\ momentum\ entrainment} + \underbrace{-\frac{1}{2}\frac{\partial {w_c}^2}{\partial z}}_{(4)\ vertical\ advection}$$

$$+ \underbrace{-\frac{1}{A_c\lfloor\rho\rfloor_c}\frac{\partial A\lfloor\rho(w-w_c)\rfloor_c^{\,2}}{\partial z}}_{(5)\ turbulent\ vertical\ flux} \qquad (1)$$

where we sample only cloudy updraft points or some subset of those points (e.g. only terminal congestus updrafts, etc.). At each vertical level, the conditionally sampled area is A_c. The conditional average is represented by the $\lfloor\ \rfloor_c$ operator, such that $\lfloor\psi\rfloor_c = \frac{\int_c \psi dC}{A_c}$. Similarly, terms with a subscript ψ_c are density-weighted conditional averages such that $\psi_c = \frac{\int_c \rho\psi dC}{A_c\rho_c}$, where ρ is the density. The full derivation of Equation (1), is shown in the appendix. The term on the left-hand side of Equation (1) is the time tendency of updraft velocity *w* for a given timestep at each vertical level. The terms on the right-hand side represent forcings that drive the vertical acceleration. The first term is the acceleration due to buoyancy ($B = g\frac{\theta'}{\theta_0} + gr_v'\frac{1-\epsilon}{\epsilon} - gr_c$), where g is the gravitational acceleration, θ is potential temperature, r_v is the water vapor mixing ratio, and r_c is the total condensate mixing ratio; specifically, this can be broken down into buoyancy due to thermal perturbations ($g\frac{\theta'}{\theta_0}$), water vapor mixing ratio perturbations ($gr_v'\frac{1-\epsilon}{\epsilon}$), and condensate loading ($-gr_c$). The second term is the acceleration due to the PPGF, where p is the pressure. The third term is entrainment of vertical momentum

into/out of the conditionally sampled area (where $\overrightarrow{v_H}$ is the horizontal wind vector), and the last two terms are the bulk and turbulent advection of vertical momentum, respectively.

The prime (') on the terms in Equation 1 denotes a perturbation calculated relative to an environmental base-state (denoted by a zero subscript). We follow a similar approach to Marinescu et al. (2021) in calculating the base-state. At each timestep, the median of all non-cloudy grid points (condensate < 0.01 g kg^{-1}) is taken at each model altitude thus comprising the environmental profile from which to calculate perturbations at each timestep. We use the median of non-cloudy grid points rather than the temporally invariant model base state, but the two are in good agreement and differ only marginally. It should be noted that at each timestep, the perturbation is taken from a single background profile rather than relative to the nearby environment of each updraft for the sake of simplifying computations, though this may cause some deviation from the actual acceleration experienced by an updraft (Davies-Jones 2003; Peters 2016).

b Composite vertical profiles

Mean vertical profiles of the terms driving the vertical velocity for each congestus type are shown in **Figure 2.8**. Over the whole congestus ensemble, buoyancy and PPGF (**Figure 2.8b-c**) have the largest magnitudes, which is consistent with many past studies of updraft momentum budgets (e.g. de Roode et al. 2012). Buoyancy and PPGF have approximately opposite trends with a slight offset in the vertical such that the PPGF acts as a drag on the buoyancy acceleration. The horizontal entrainment of momentum is close to zero (**Figure 2.8e**). Turbulence and vertical advection of momentum (**Figure 2.8f-g**) generally have smaller magnitudes than buoyancy and PPGF throughout the column, but have appreciable magnitudes nearing the 0°C level and above.

Although buoyancy and PPGF account for the largest magnitudes of updraft acceleration, their sum does not fully describe the shape of the vertical velocity profile. Positive net accelerations would generally lead to increases in vertical velocity with height, with the opposite for negative accelerations. The combination of buoyancy and PPGF (**Figure 2.8d**) does not match up with the turning points in the vertical velocity profile (**Figure 2.8a**), which are drawn as gray lines to guide the reader. Instead, accounting for the acceleration due to vertical advection (both bulk advection in **Figure 2.8g** and sub-plume fluctuations in **Figure 2.8f**) leads to a better alignment with the mean updraft profile (**Figure 2.8h**).

As shown previously, mature transient congestus have stronger updrafts than terminal congestus all throughout the column (**Figure 2.8a**). On the other hand, developing transient congestus only have stronger updrafts than terminal congestus above 2.7km AGL (**Figure 2.9a**). This increase in developing transient updraft velocity occurs alongside an increase in buoyancy relative to terminal congestus (especially thermal buoyancy, as shown in **Figure 2.9b-c**). This adds support to earlier findings that environments favoring more buoyant updrafts tend to produce more transient congestus (Redelsperger et al. 2002; Takemi et al. 2004; Jensen and Del Genio 2006). Although a combination of acceleration terms is needed to fully describe the shape of the vertical velocity profile, buoyancy is the primary driver of those congestus which are able to ascend through the 0°C level.

c Composite cross-sections

We have shown that directly below the 0°C level, transient congestus tend to be more buoyant than terminal congestus, which allows them to continue developing vertically through the 0°C stable layer. In order to improve our physical understanding as to why this is the case, we

construct combined vertical and radial composites to examine the horizontal structure of the updraft and its interactions with the surrounding environment.

Figure 2.10 shows composite cross-sections of total condensate, vertical velocity, cross-cloud edge velocity, and latent heat released as a result of vapor to liquid transitions for terminal, developing transient, and mature transient updrafts. The vertical axis corresponds to altitude. The horizontal axis represents normalized distance from the cloud edge, with the cloud edge located at r*=0 (black dashed line), the in-cloud points located to the left of r*=0 (black dashed line), and the environmental points to the right of r*=0. Wind barbs show the mean circulation through the updraft. It is evident that updraft velocity and condensate tend to decrease moving radially outwards from the center **(Figure 2.9a-f)**, which is consistent with a switch from net latent heat release within the updraft core arising from condensation and cloud droplet activation (warm colors in **Figure 2.10j-l**), to net latent heat absorption outside the updraft due to evaporation (cool colors in **Figure 2.10j-l**).

Directly surrounding the updraft, there is a shell of subsiding air that is narrower than the updraft itself (**Figure 2.10d-f**). The strongest downdrafts occur just below the level of cloud top, at the altitude of maximum updraft velocity, a feature also observed by Savre (2021). The shape of the subsiding shell is consistent with vortex dynamics and numerous other studies focused on such effects (Sherwood et al. 2013; Romps and Charn 2015; Peters et al. 2019; Savre 2021). The composite wind field shows the updraft and downdraft as part of a circulation with entrainment near cloud base and detrainment towards cloud top (**Figure 2.10g-i**). Closer to the updraft core, mean winds are directed towards the updraft core as high ~3-4km AGL.

Overall, mature transient congestus have faster updraft velocities **(Figure 2.10d,f)** and more condensate mass **(Figure 2.10a,c)** than terminal congestus. The differing height relative to

the 0ºC level also strongly impacts the subsiding shell. Terminal congestus downdraft shells are more column-shaped, extending fairly continuously until close to cloud base **(Figure 2.10d**). Mature transient congestus have more of a vortex-driven structure, with a strong downdraft at cloud top height to just above the 0℃ level and weaker downdrafts below. The updraft circulation is broken up by the stable layer to form distinct circulations above and below the 0℃ level **(Figure 2.10i**). Similar large-scale circulations around the 0℃ level were also seen in Posselt et al. 2008.

To further investigate why terminal congestus tend to be less buoyant than developing transient congestus above 2.7km AGL (as shown in **Figure 2.9**), and thus why developing transient congestus are ultimately able to extend past the 0℃ level, we compare their cross-sections of various properties in **Figure 2.11.** Looking at these cross-sections allows us to identify differences not only within the updraft, but also between the environments in which the two types of congestus develop.

Transient congestus tend to develop in more humid environments ($r^*>2$ in **Figure 2.11c**), particularly above ~2km AGL. At corresponding altitudes, terminal congestus experience more evaporation of cloud droplets (**Figure 2.11f**) alongside a drop in buoyancy relative to transient congestus (**Figure 2.9b-c**). This suggests that transient congestus are more protected from dilution in the midlevels between ~3km AGL and the 0℃ level, explaining their faster updraft velocities in this region (**Figure 2.9a**). Transient congestus updrafts are mixed with more humid environmental air, leading to less droplet evaporation and greater buoyancy compared to terminal congestus at the same altitudes. The importance of humidity between the trade wind and 0℃ level stable layers supports previous research (e.g., Redelsperger et al. 2002) that found midlevel dry layers to be the most important environmental factor determining congestus height.

This effect is compounded by transient congestus being wider than terminal congestus at those altitudes **(Figure 2.6b**), which further protects their updraft cores from dilution. The difference in equivalent potential temperature (θ_e) is shown in **Figure 2.11j-l** as a metric for dilution, with larger θ_e values correspond to air originating from the surface, and decreases in θ_e from cloud base to cloud top being reflective of environmental air mixing into the updrafts. Comparing the terminal and developing transient congestus shows that terminal congestus tend to be more diluted (**Figure 2.11l**), particularly above ~2.7km where the substantial differences in updraft width contribute to differences in buoyancy dilution and thereby overall vertical momentum.

The increase in updraft velocities below the 0℃ level allows developing transient congestus to activate and maintain more cloud condensate as they encounter the 0℃ stable layer (**Figure 2.11i**, **Figure 2.6c**). As mature transient congestus cross the 0℃ level, they do still experience a dip in buoyancy as a result of the increased condensate loading and the decreased thermal buoyancy (dark blue line in **Figure 2.8b**). However, upon crossing the 0℃ level, the condensate can start to freeze and release latent heat (**Figure 2.10o)**, which allows them to regain some buoyancy (**Figure 2.8b**) and continue developing vertically.

2.5 Aerosol activation and detrainment

The differences in vertical development between terminal and transient congestus as discussed in Section 2.4 lead to differences in cloud top height relative to the 0ºC level. In this section, we examine the effects of those differences on the convective transport of water vapor and aerosol particles. RAMS aerosol budget capabilities (Saleeby and van den Heever 2013) allow us to track how aerosol particles within the model domain interact with, and are redistributed by, congestus updrafts. **Figure 2.13** shows composites of water vapor and three

separately tracked terms within the aerosol budget taken as perturbations from the clear-sky mean at the same timestep. Aerosol particles are initialized in the *unprocessed* aerosol term. When they are activated as CCN in cloud droplets, the aerosol mass is transferred to the *in-hydrometeor* aerosol term. As those hydrometeor droplets evaporate under subsaturated conditions, the aerosol mass contained in those droplets is returned to the domain in the *regenerated* aerosol term.

Transient and terminal congestus have similar patterns of the surrounding aerosol fields: unprocessed aerosol concentrations are lower around and within congestus updrafts, as those aerosol particles are activated as CCN and are subsequently transferred to the in-hydrometeor category. A majority of aerosols enter the updraft at cloud base at the entraining branch of the overturning circulation involving the updraft and its surrounding shell **(Figure 2.12a,b**). For transient congestus though, which extend above the 0°C level, the overturning circulation is broken into two circulations, one above and one below the 0°C stable level (**Figure 2.10f,i**). As a result, there is also entrainment into the updraft at the 0°C level for mature transient congestus **(Figure 2.12b**). This entrainment of aerosol particles around stable layers has implications for what air masses are entrained into clouds, especially in regions with vertical inhomogeneity in aerosol or water vapor concentrations.

Once the aerosol enters the updraft, it activates cloud droplets and enters the in-hydrometeor aerosol category (**Figure 2.12d-e**). Most aerosol particles are activated within 2 km above cloud base, with more being activated towards the center of the updraft, where updraft velocities are highest and the concomitant production in supersaturation is greatest, compared with the outer regions of the updraft. Transient congestus activate more aerosol particles than

terminal congestus throughout most of the column (**Figure 2.12f**), due to their stronger updraft velocities producing higher supersaturations.

Aerosol particles are regenerated, and returned to the atmosphere, along cloud edges where the updraft is weak and supersaturation is insufficient to activate available CCN and condense water onto existing droplets. Hence, evaporation dominates (**Figure 2.12 g-h**). Once the liquid water is evaporated the aerosol particles are returned to the subsaturated environment. As the droplets evaporate, water vapor is also enhanced relative to the clear-sky background (**Figure 2.12 j-k**). Most aerosol is regenerated near cloud top and along the edges of the updraft which is in keeping with the fact that these regions of the cloud are more susceptible to dry air entrainment and mixing, and hence evaporation. Around the cloud edges, terminal congestus evaporate more readily (**Figure 2.11j**) upon mixing with their less humid environments (**Figure 2.11a**), compared to transient congestus. As a result, they subsequently release more regenerated aerosol than transient congestus (**Figure 2.12**i).

Transient congestus also regenerate notable aerosol mass within the updraft above the 0°C level (**Figure 2.12h**), despite being buoyant with a positive acceleration at those altitudes (**Figure 2.8b, g**), and an associated net release of latent heat (**Figure 2.10l**). This increase in regeneration may be attributed to reductions in updraft velocity and hence the generation of supersaturation after penetrating the 0°C stable layer. Regeneration may further be increased in the transition from warm to mixed phase regions as ice nucleation begins, and liquid water is evaporated and lost to ice through the Wegner-Bergeron-Findeisen process (Verheggen et al. 2007; Engström et al. 2008; Corr et al. 2016). These returned or regenerated aerosol particles are transported outward in the detraining layer, as well as downward in the subsiding shell. This

detrainment of aerosol particles lead to enhanced aerosol concentrations as far as two updraft radii away from the updraft edge (~2-4km away).

Although transient congestus have comparatively stronger downdrafts than terminal congestus at their respective cloud top heights (**Figure 2.10d, f**), terminal congestus downdrafts extend all the way to cloud base, while mature transient congestus downdrafts are broken up by the 0℃ stable layer. *As a result, terminal congestus have greater amounts of regenerated aerosol between the surface and 3km (**Figure 2.12i**), while transient congestus have greater regenerated aerosol and water vapor in midlevel detrainment layers*. The aerosol and water vapor being detrained above the 0℃ stable layer in mature transient congestus clouds are less able to be transported to the surface by virtue of the presence of the stable layer, and a local maximum of aerosol and water vapor is formed around the 0℃ level. This has significant implications for subsequent aerosol activation and the formation of cloud droplets in altocumulus clouds. This also emphasizes the role of congestus detrainment in modifying the near-cloud environment, as well as the manner in which the heights of terminal and transient congestus relative to stable layers influence this modification.

2.6 Discussion and conclusions

Despite the importance of cumulus congestus as a mode of tropical convection, relatively little is understood about what causes some congestus to be capped by the 0℃ stable layer (i.e. terminal) while others are able to penetrate the 0℃ stable layer and continue to develop vertically (i.e. transient). With the goal of enhancing our scientific understanding of congestus updraft processes, we conducted high-resolution large eddy simulations of an idealized congestus cloud field and created composites of congestus properties in both the vertical and radial dimensions. The use of tobac, an object-tracking algorithm, allowed for updrafts to be tracked in

time thereby providing a more accurate comparison of terminal versus transient congestus processes than afforded by domain averages or other bulk analyses.

We first examined the physical mechanisms that govern the updraft acceleration budget of congestus clouds. The balance between buoyancy and perturbation pressure gradient accelerations was shown to describe the shape of the updraft vertical velocity profiles better than either term alone. We also showed that accounting for vertical advection of momentum throughout bulk and turbulent motions improved the representation of the overall vertical velocity profile than simply considering the sum of the buoyancy and PPGF.

We demonstrated that transient congestus have stronger updrafts and higher cloud tops than terminal congestus. Despite these differences, both types of congestus have similarly structured updrafts characterized by an overturning circulation between the updraft and surrounding subsiding shell. A conceptual schematic depicting the overturning circulations of terminal and transient congestus is shown in **Figure 2.13**. Terminal and transient congestus updrafts are both surrounded by relatively weaker downdrafts, though terminal congestus downdrafts are more vertically homogenous and extend all the way to cloud base. Transient congestus downdrafts on the other hand have stronger maxima above the 0ºC level, and the overturning circulation is broken up into distinct branches separated by the 0℃ stable layer in addition to the branches separated by the trade wind stable layer.

In analyzing which factors of the vertical acceleration budget predominantly influenced the differences between the two types of congestus, we have shown that buoyancy is essential for distinguishing between transient and terminal congestus. This supports previous work that found strong correlations between environments favoring more buoyant updrafts and taller congestus (Jensen and Del Genio 2006; Redelsperger et al. 2002). We established a physical mechanism for

this process by showing that transient congestus are surrounded by more humid environments above 2.7km AGL, which corresponds to more protection from evaporation, increased buoyancy, and ultimately increased vertical velocity near the 0°C level relative to terminal congestus.

Finally, aerosol budget tracking and compositing allowed us to describe how detrainment from congestus updrafts influenced their near-cloud environments, including aerosol loading. Transient congestus ingest more aerosols due to their increased updraft velocities. Terminal congestus regenerate more aerosol along their edges due to increased evaporation as a result of their drier environments. However, beyond the subsiding shell, transient congestus have a larger contribution to midlevel aerosol layers, as they detrain aerosols above the 0°C stable layer and rapidly transport it radially outwards, rather than directly towards the surface due to constraints imposed by the 0°C stable layer. By virtue of both of these different water vapor and aerosol detrainment circulations, the ratio of terminal to transient congestus within an environment therefore has implications for the location and development of mid-level clouds such as altocumulus.

It should be cautioned that the results of this study, while based on a large population of congestus updrafts at varying stages of their life cycle, only describe one tropical maritime environment. The environment influences the vertical structure of the congestus and the proportion of terminal to transient congestus. It would be interesting to utilize the vertical acceleration framework used in this study to examine how the balance between buoyancy, PPGF, and vertical momentum advection changes with environmental properties such as the strength of the 0ºC stable layer, mid-level humidity, wind shear, and even the vertical gradient of aerosol concentration. Furthermore, the aerosol composites from this study suggest that environments with differing proportions of transient congestus, as has been shown for increased surface aerosol

loadings in Sheffield et al. (2015), are likely to have differences in midlevel aerosol and water vapor detrainment layers. This is an ongoing area of research by the authors, and the results presented in this study will serve as a valuable control simulation to better understand how congestus updrafts vary in differing thermodynamic and aerosol environments.

2.7 Tables

Table 2.1. RAMS model options used in simulation.

Model Aspect	**Setting**
Grid	Arakawa C grid
	1000 x 1000 points, $\Delta x = \Delta y = 100m$
	120 vertical levels, $\Delta z = 50 - 200\ m$
Time integration	48 hour simulation duration, $\Delta t = 0.75s$
Initialization	Horizontally homogenous thermodynamic and wind profile, averaged from ERA-5 and CAMP^{2}Ex dropsonde
	Random potential temperature perturbations within the lowest 500m AGL of the domain, with a maximum perturbation of 0.1K
Surface scheme	All-ocean surface with fixed sea surface temperature (SST)
	LEAF-3 (Walko et al., 2000)
Boundary conditions	Periodic in zonal and meridional directions
Microphysics scheme	Two-moment bulk microphysics (Meyers et al. 1997)
	8 hydrometeor classes (Saleeby and Cotton 2004)
	Heterogenous ice nucleation (DeMott et al. 2010)
Radiation scheme	Two-stream, hydrometeor sensitive (Harrington, 1997)
	Updated every 5 minutes
Aerosol treatment	Ammonium sulfate aerosol, with single log-normal mode

	Maximum concentration (CCN: 500 mg^{-1}, IN: 0.01 mg^{-1}) at the surface and exponentially decreasing with altitude
	Aerosol-radiation interactions on
	Aerosol sources and sinks on, with full aerosol budget tracking (Saleeby and van den Heever 2013)

2.8 Figures

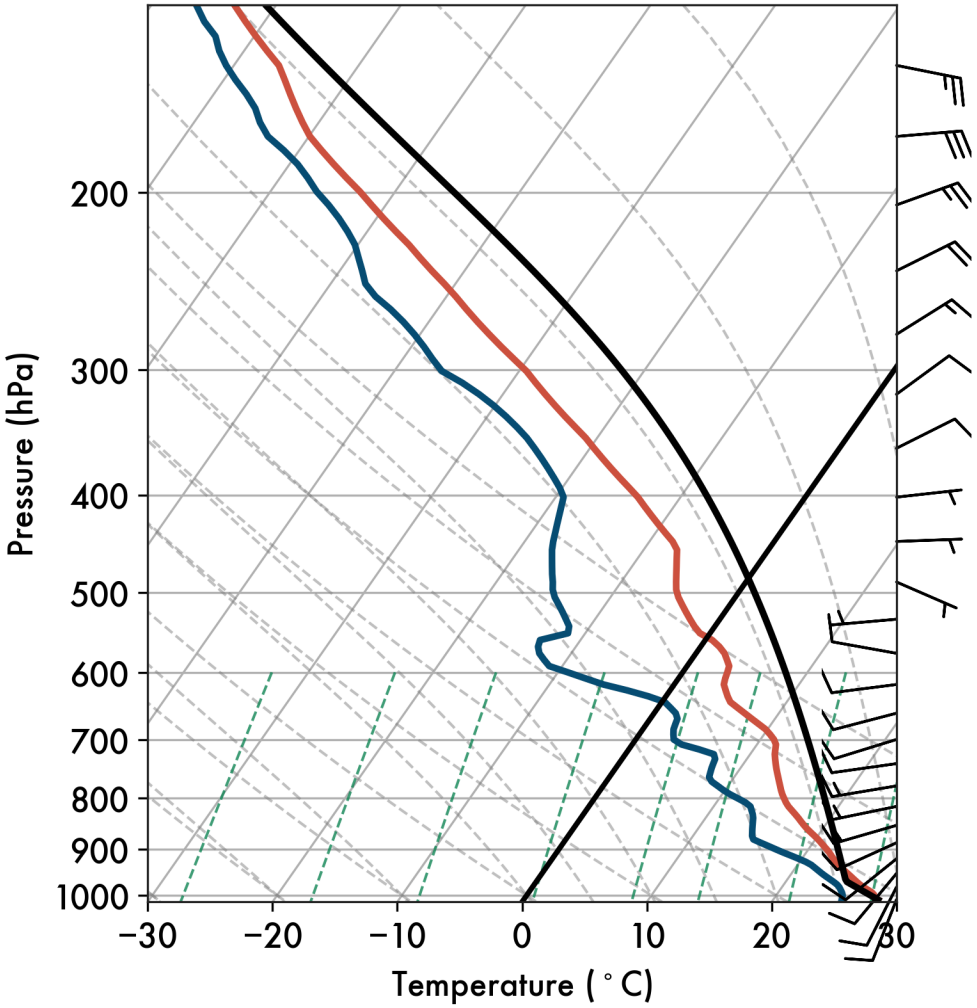

Figure 2.1. Skew*T* – log*p* diagram showing the sounding and wind profile (m s^{-1}) used to initialize the numerical experiments. The black diagonal line indicates the freezing level. The solid black curve is a parcel trajectory from the surface.

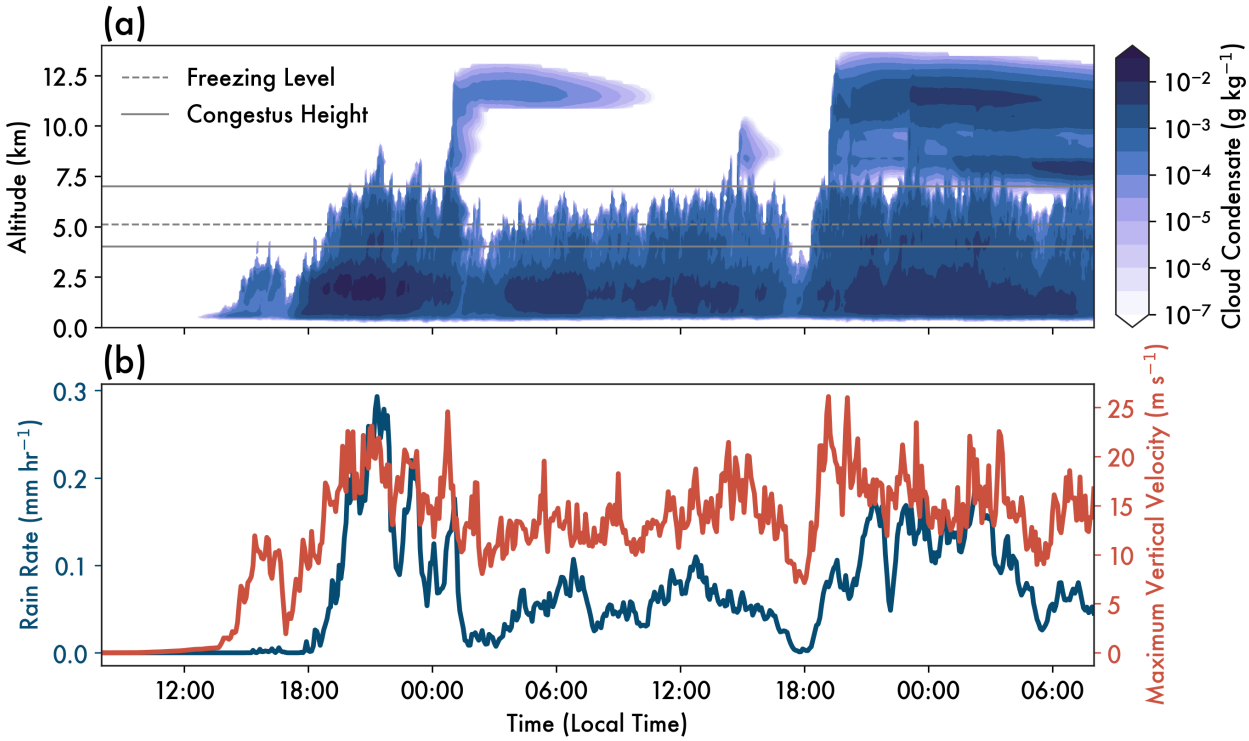

Figure 2.2. Mean evolution of the trimodal convective cloud development over the course of the simulation, showing (a) domain-mean cloud condensate (g kg^{-1}) and (b) mean precipitation rate (mm hr^{-1}) (blue) and maximum updraft velocity (m s^{-1}) (red). In (a), the 0°C level is indicated by the dashed black horizontal line, and congestus height criteria (4-7km AGL) are indicated by the solid gray horizontal lines. The simulation began at 0 UTC (8am LT). The first 7.5 hours of the simulation are considered spin-up time and are not included in the figure or the analysis.

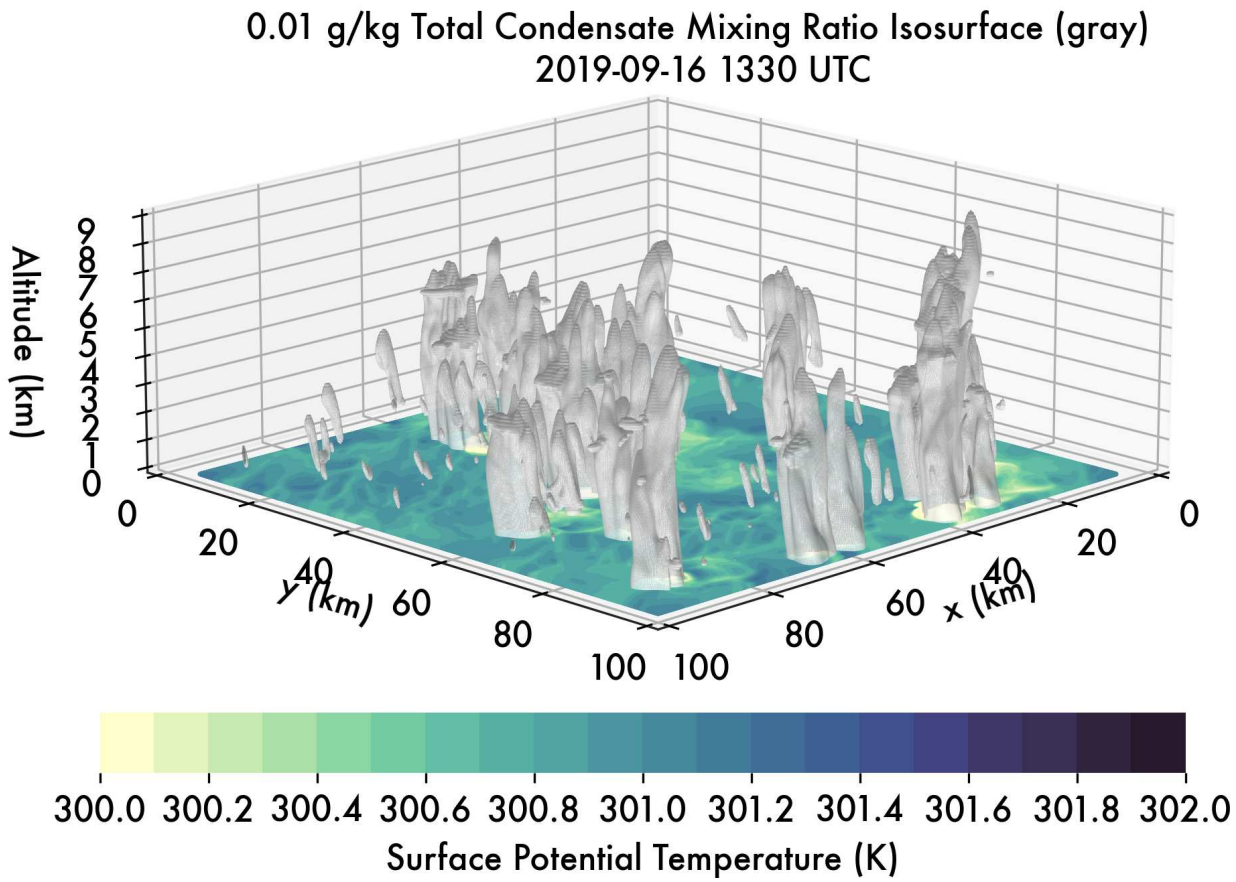

Figure 2.3. Three-dimensional snapshot of the cumulus and congestus cloud field at 13:30 UTC (21:30 LT). Gray isosurfaces are 0.01 g kg^{-1} of cloud condensate. Surface colors are the potential temperature at the lowest above-surface model level and show the development of cold pools in association with the congestus.

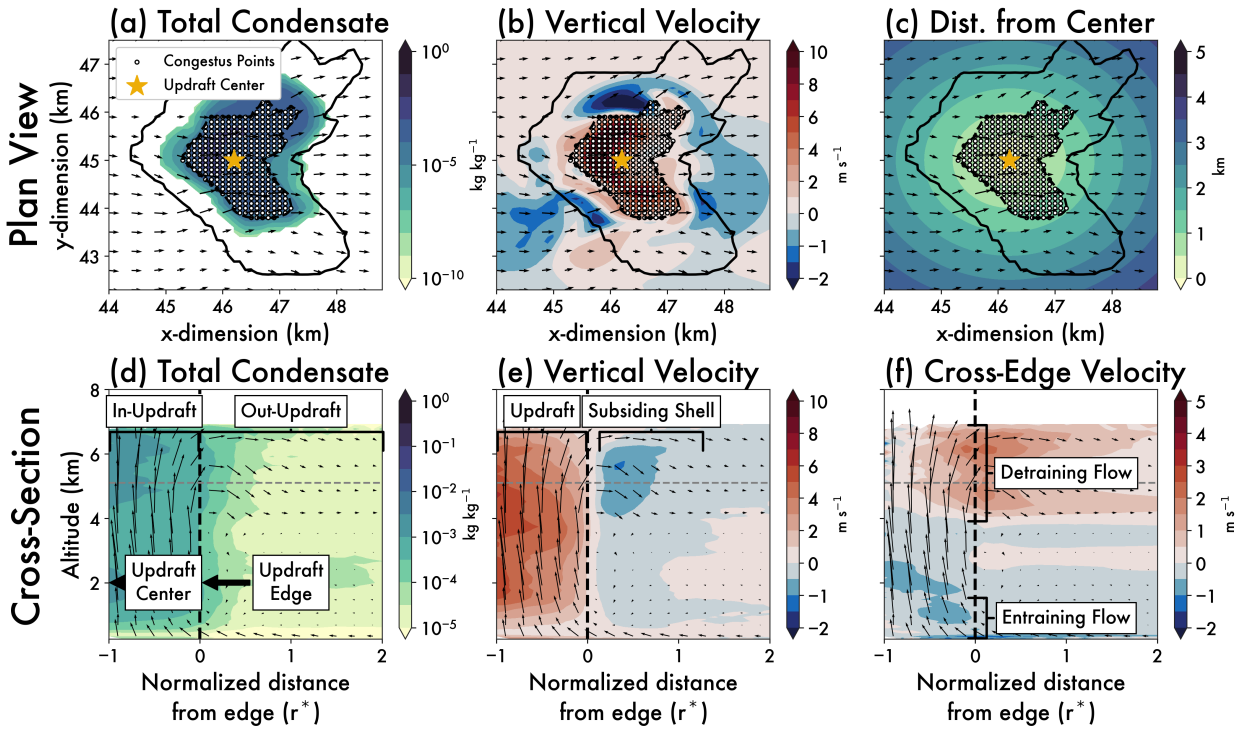

Figure 2.4. Definition of the normalized radial coordinates and composite cross-sections. Top row (a-c) show a plan view of a single updraft, where the yellow star is the updraft center, and small black dots represent congestus updraft points as identified by the criteria described in text. Dashed gray contours are the updraft edge (r*=0) and solid contours are one radius away (r*=1) from the updraft edge. Horizontal wind barbs are also displayed. Bottom row (d-f) shows a composite cross-section through all congestus updrafts as a function of altitude and normalized distance from the updraft edge (r*=0), with key aspects of the overall flow annotated. The vertical dashed black line is the updraft edge. The horizontal dashed gray line is the mean 0°C level. Vertical and cross-edge wind barbs are displayed. Note that the color scales for total condensate in panel (a) and (d) are different.

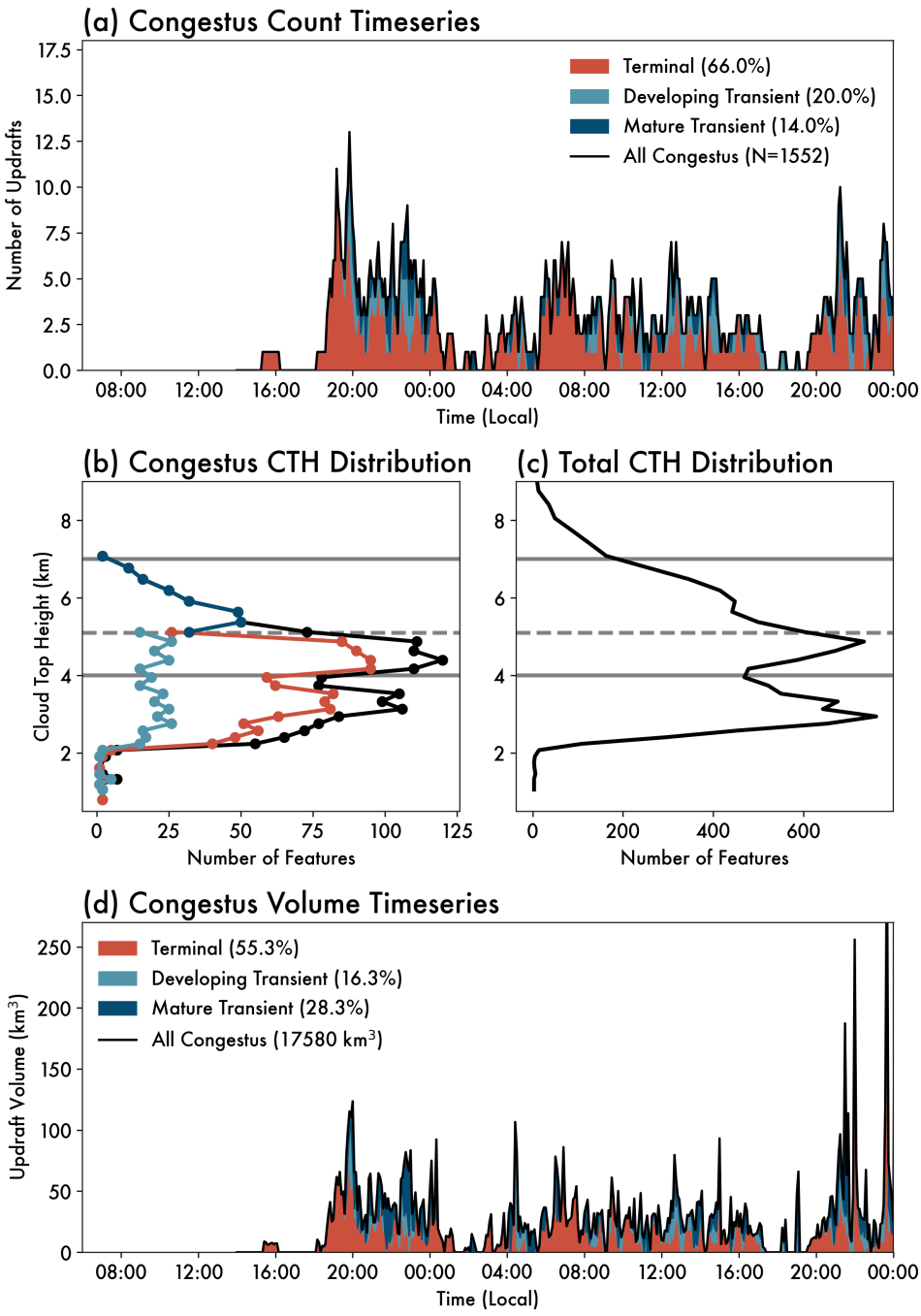

Figure 2.5. The characteristics of the congestus in this study as shown by (a) a timeseries of the number of identified congestus updrafts separated into terminal (red), developing transient (light blue), and mature transient (dark blue) clouds. The colored regions show the relative contributions of each category to the total number of congestus (black line). Histograms of (b) congestus cloud top heights at each timestep and (c) full cloud top height distribution over entire analysis period, with colors in (b) corresponding to the categories shown in (a). (d) A timeseries of the total volume occupied by each type of updraft. The 0°C level is indicated by the dashed gray horizontal line, and congestus height criteria (4-7km AGL) are indicated by the solid gray horizontal lines.

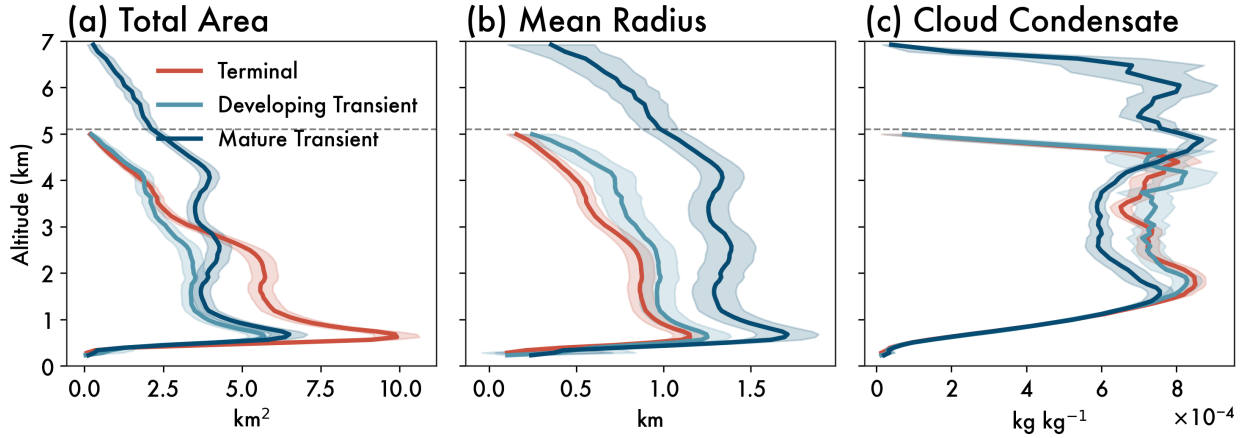

Figure 2.6. (a) Total area occupied (km^2), (b) mean effective updraft radius (km), and (c) mean cloud condensate (kg kg^{-1}) for terminal (red), developing transient (light blue), and mature transient (dark blue) congestus. Solid lines are the mean and the shaded areas are the 5th to 95th percent confidence intervals at each vertical level.

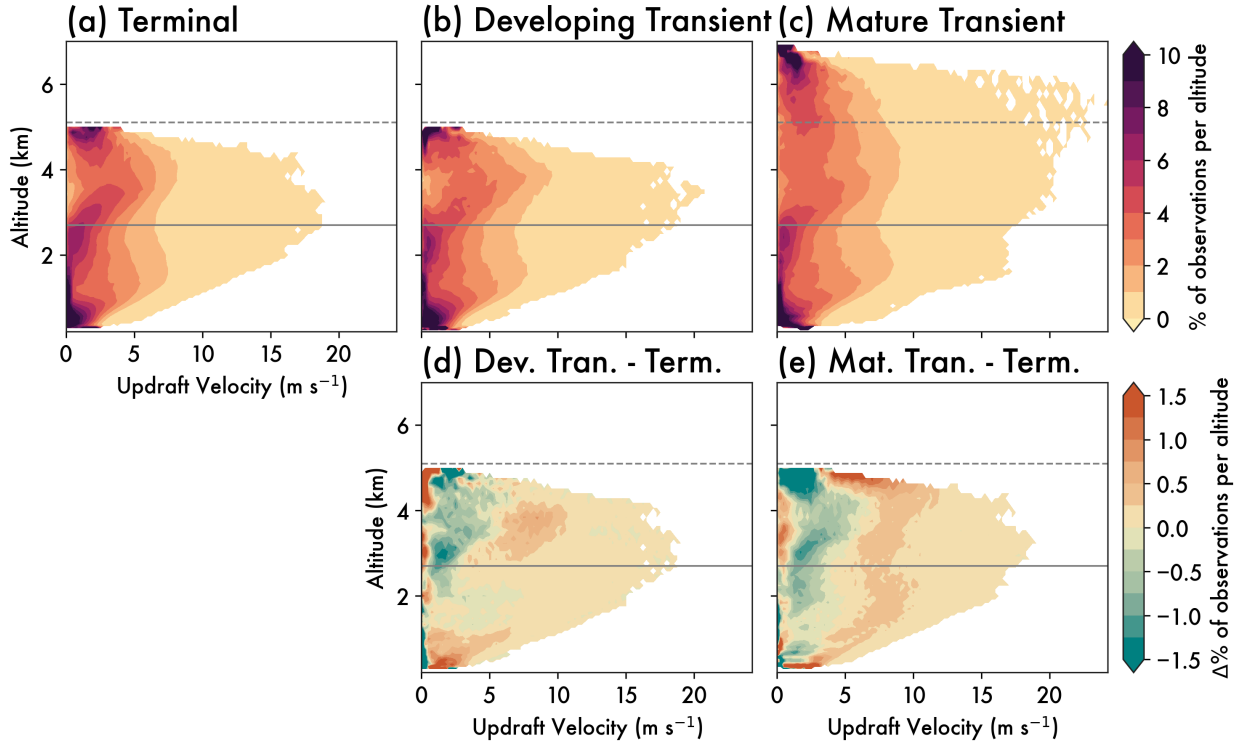

Figure 2.7. Contoured frequency by altitude diagrams (CFADs) of updraft velocity (m s^{-1}) as a function of altitude (km), for (a) terminal, (b) developing transient, and (c) mature transient congestus. (d-e) show the difference in percent of the developing and mature transient congestus relative to terminal congestus. Note that altitudes above 5.1km in (d-e) have been left blank because there are no terminal congestus above that altitude, as defined in text. The horizontal dashed gray line indicates the mean 0°C level, and the solid gray line indicates 2.7km AGL as discussed in text.

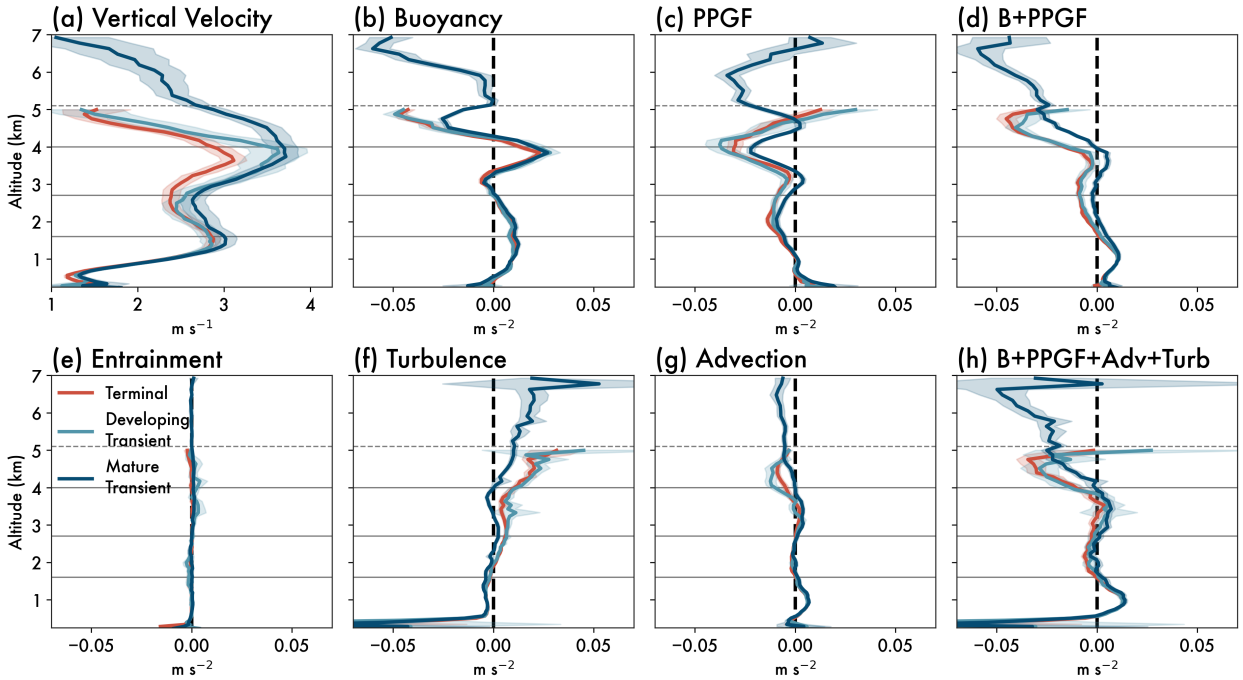

Figure 2.8. Profiles of vertical velocity and the terms primarily contributing to the updraft acceleration for terminal (red), developing transient (light blue), and mature transient (dark blue) congestus. Lines represent mean vertical profiles of (a) vertical velocity (m s^{-1}), (b) buoyancy acceleration, (c) PPGF acceleration, (d) the sum of buoyancy and PPGF accelerations, (e) horizontal entrainment acceleration, (f) turbulent vertical advective acceleration, (g) bulk vertical advective acceleration, and (h) the sum of buoyancy, PPGF acceleration, turbulent, and vertical advective acceleration (all in m s^{-2}), as a function of altitude (km). Shaded areas cover the 5th through 95th confidence intervals at each level. The horizontal dashed line denotes the mean 0ºC level, while the horizontal solid lines correspond to levels where the first derivative of vertical velocity changes sign.

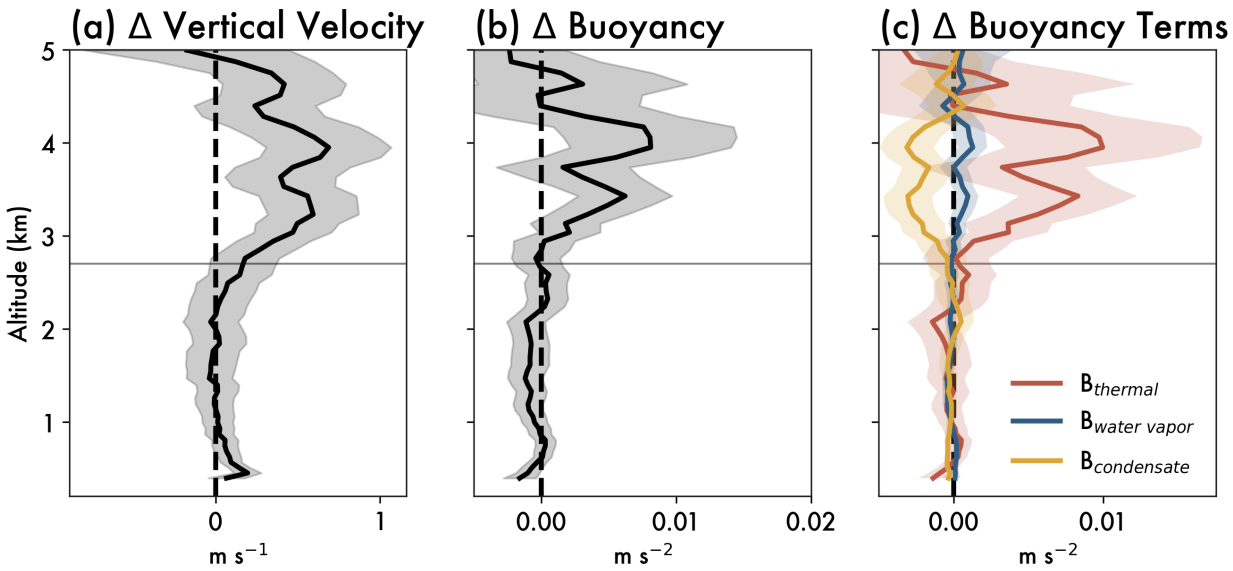

Figure 2.9. Difference profiles of developing transient and terminal congestus in terms of (a) vertical velocity (m s^{-1}), (b) buoyancy (m s^{-2}), and (c) individual buoyancy terms (m s^{-2}). Shaded areas cover the 5th through 95th confidence intervals at each level. Horizontal solid gray line indicates 2.7km AGL, as described in text.

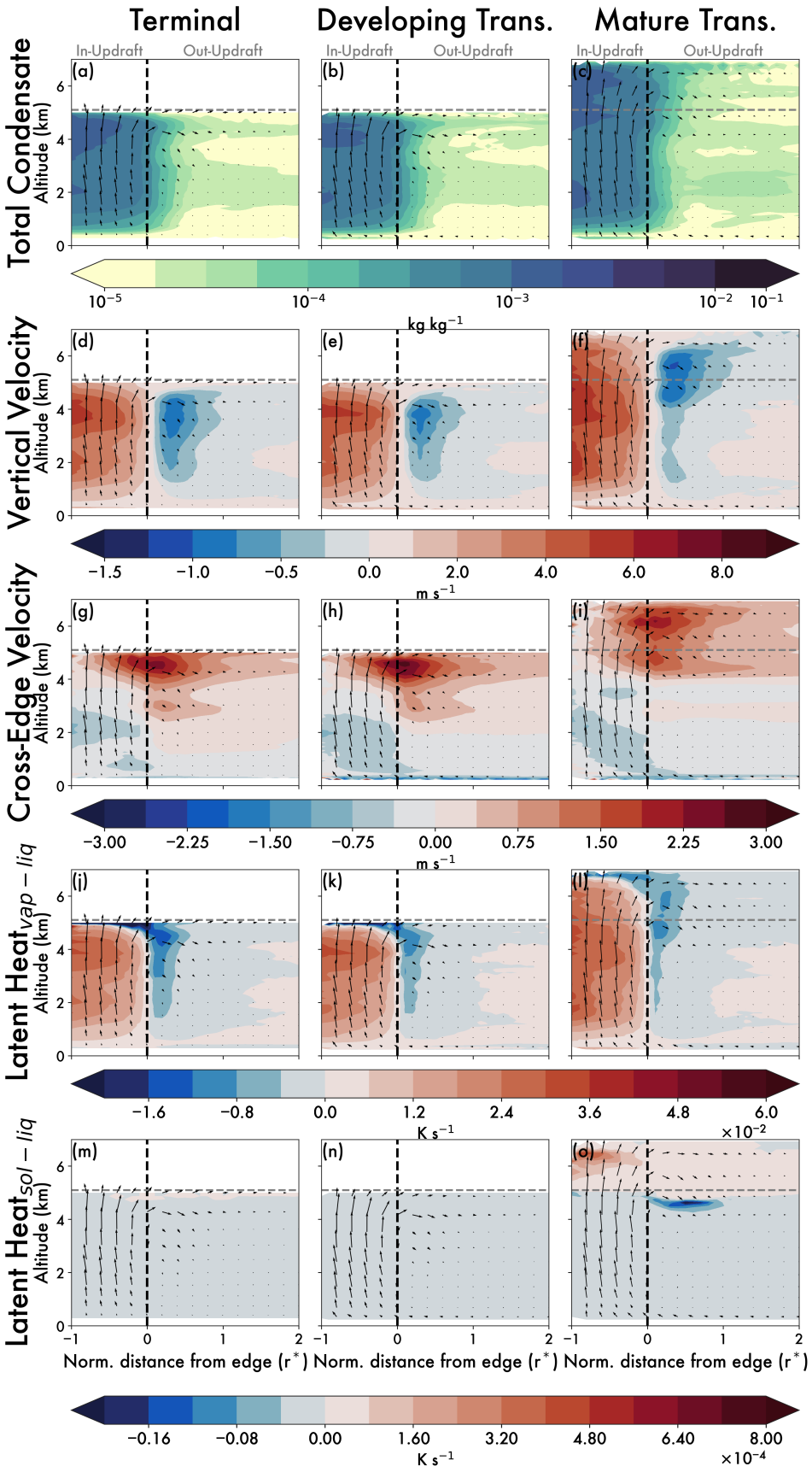
Terminal
Developing Trans.
Mature Trans.
In-Updraft
Out-Updraft
(a)
(b)
(c)
(d)
(e)
(f)
(g)
(h)
(i)
(j)
(k)
(l)
(m)
(n)
(o)
Total Condensate
Vertical Velocity
Cross-Edge Velocity
Latent Heat$_{vap-liq}$
Latent Heat$_{sol-liq}$
Altitude (km)
kg kg^{-1}
m s^{-1}
K s^{-1}
×10^{-2}
×10^{-4}
Norm. distance from edge (r*)

Figure 2.10. Composite congestus updraft cross-sections of (a-c) total condensate (kg kg^{-1}), (d-f) vertical velocity (m s^{-1}), (g-i) cross-edge velocity (m s^{-1}), (j-l) latent heat due to vapor-liquid transitions (K s^{-1}), and (m-p) latent heat due to solid-liquid transitions (K s^{-1}) as a function of the normalized distance from core edge (r*) and altitude. The left column is a composite of terminal congestus, the middle column is a composite of developing transient congestus, and the right column is a composite of mature transient congestus. The wind barbs show mean vertical and cross-edge flow relative to clear-sky conditions. The black vertical dashed line at r*=0 denotes the mean edge of the updraft. Only coordinates with more than 50 samples are shown. Areas above 5.1km AGL are left blank in the left and middle columns since terminal congestus and developing transient congestus are defined to have cloud tops below the 0ºC level (denoted by the horizontal dashed gray line).

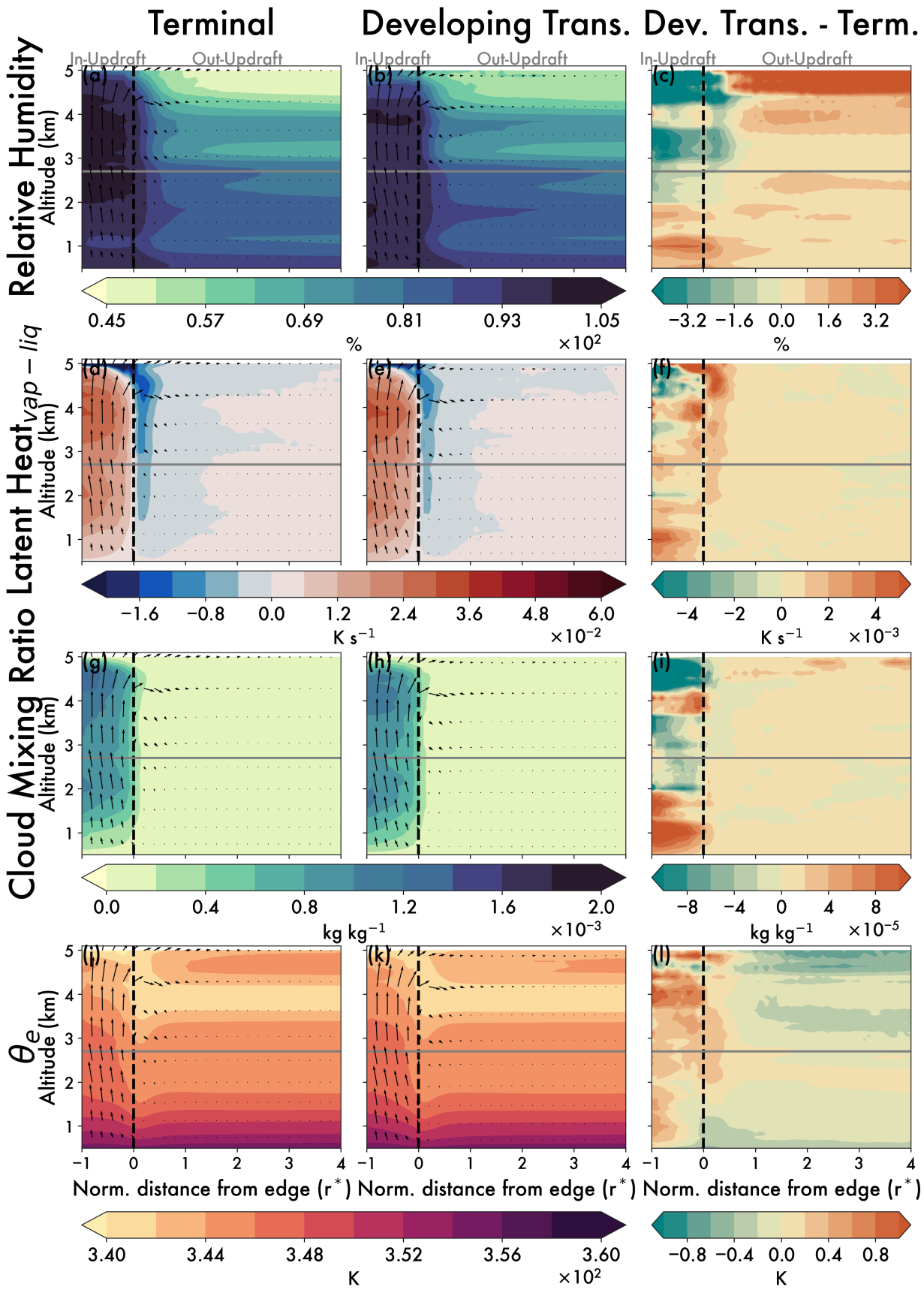
Terminal
Developing Trans.
Dev. Trans. - Term.
In-Updraft
Out-Updraft
Relative Humidity
Cloud Mixing Ratio
Latent Heat$_{vap-liq}$
θ_e
Altitude (km)
(a)
(b)
(c)
(d)
(e)
(f)
(g)
(h)
(i)
(j)
(k)
(l)
0.45 0.57 0.69 0.81 0.93 1.05
%
×10^2
−3.2 −1.6 0.0 1.6 3.2
%
−1.6 −0.8 0.0 1.2 2.4 3.6 4.8 6.0
K s^{-1}
×10^{-2}
−4 −2 0 2 4
K s^{-1}
×10^{-3}
0.0 0.4 0.8 1.2 1.6 2.0
kg kg^{-1}
×10^{-3}
−8 −4 0 4 8
kg kg^{-1}
×10^{-5}
Norm. distance from edge (r*)
3.40 3.44 3.48 3.52 3.56 3.60
K
×10^2
−0.8 −0.4 0.0 0.4 0.8
K

Figure 2.11. As in Figure 2.10, but comparing the development of terminal and developing transient congestus in terms of (a-c) relative humidity (%), (d-f) latent heat from vapor-liquid transitions (K s^{-1}), (g-i) cloud mixing ratio (kg kg^{-1}), and (j-l) equivalent potential temperature (K). Only altitudes up to 5.1km AGL are shown since only terminal and developing transient congestus are depicted. The horizontal solid gray line denotes an altitude of 2.7km AGL as described in text.

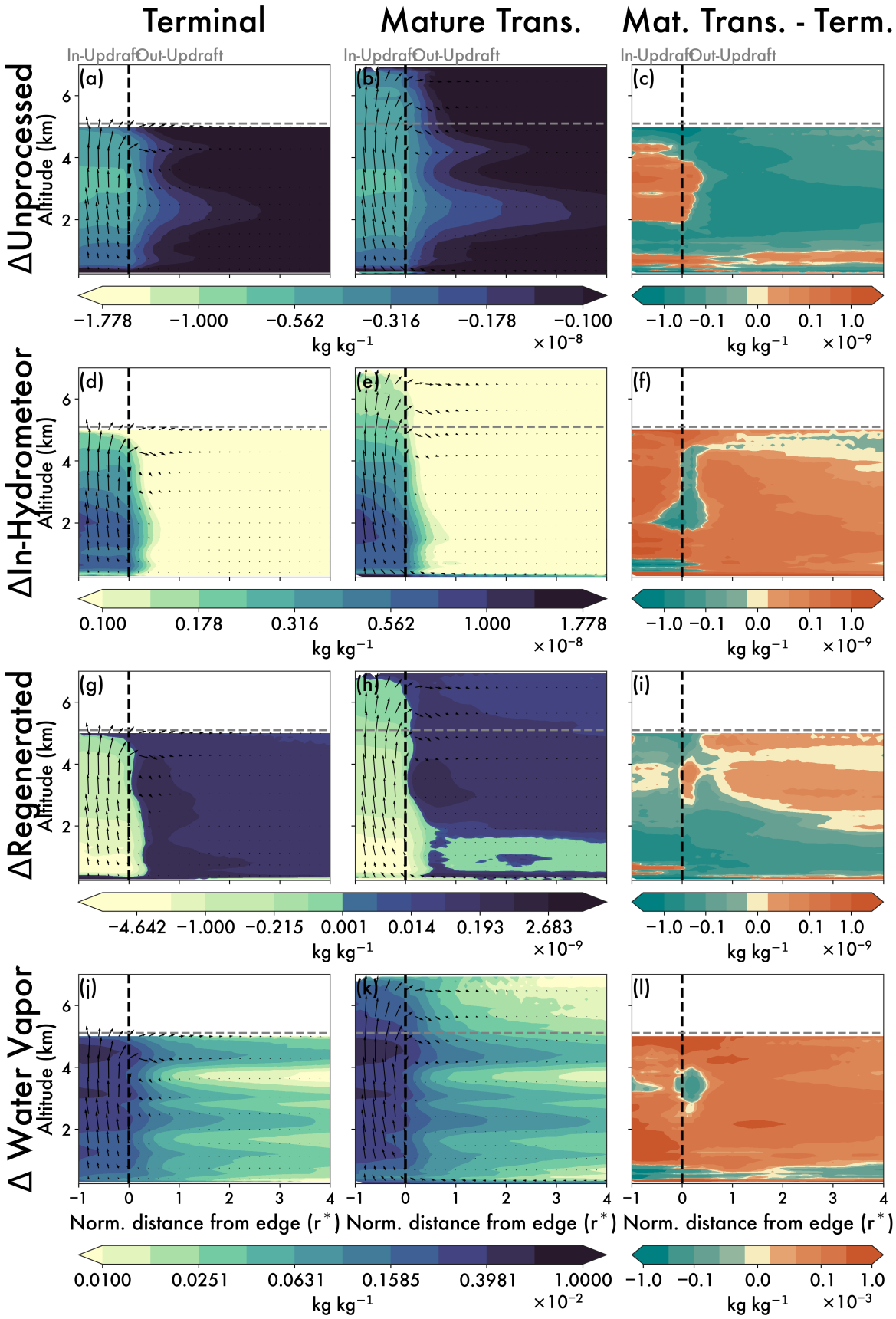
Terminal
Mature Trans.
Mat. Trans. - Term.
In-Updraft
Out-Updraft
ΔUnprocessed
ΔIn-Hydrometeor
ΔRegenerated
Δ Water Vapor
Altitude (km)
(a)
(b)
(c)
(d)
(e)
(f)
(g)
(h)
(i)
(j)
(k)
(l)
−1.778 −1.000 −0.562 −0.316 −0.178 −0.100
kg kg^{-1} ×10^{-8}
−1.0 −0.1 0.0 0.1 1.0
kg kg^{-1} ×10^{-9}
0.100 0.178 0.316 0.562 1.000 1.778
kg kg^{-1} ×10^{-8}
−4.642 −1.000 −0.215 0.001 0.014 0.193 2.683
kg kg^{-1} ×10^{-9}
Norm. distance from edge (r*)
0.0100 0.0251 0.0631 0.1585 0.3981 1.0000
kg kg^{-1} ×10^{-2}
−1.0 −0.1 0.0 0.1 1.0
kg kg^{-1} ×10^{-3}

Figure 2.12. As in Figure 2.11, but for the aerosol budget terms described in the text (kg kg^{-1}), as well as the water vapor enhancements (kg kg^{-1}). Enhancements are taken relative to clear-sky profiles at each timestep. The left column is a composite of terminal congestus, the middle column is a composite of mature transient congestus, and the right column is the difference between the middle and left columns. Areas above 5.1km in the difference plot are left blank since terminal congestus are defined to have tops below 5.1km. The gray dashed line indicates the mean 0ºC level.

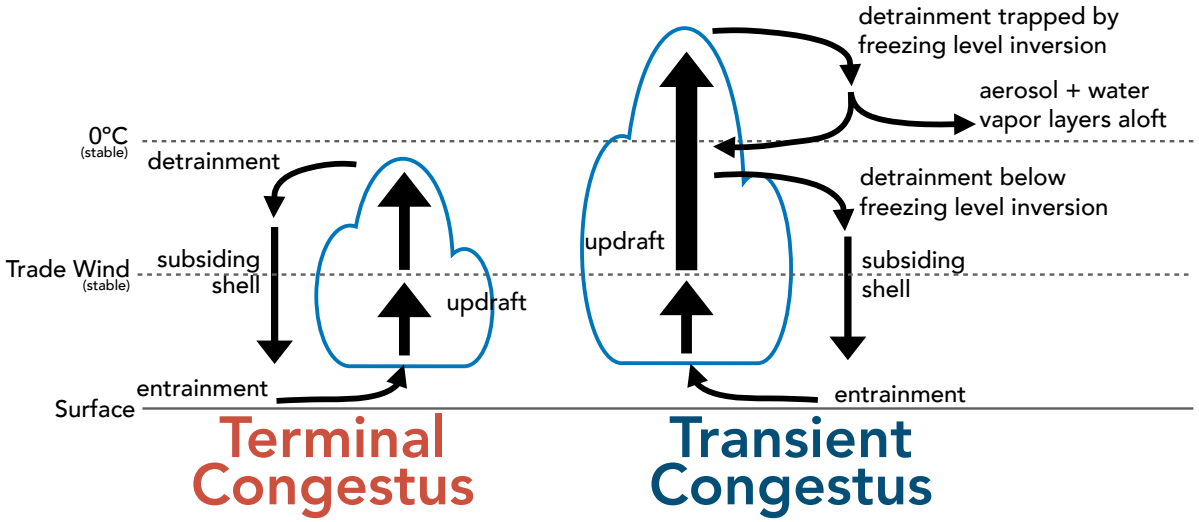

Figure 2.13. Schematic representing a conceptual model of the differences in updraft and downdraft circulations and the associated detrainment processes of terminal and transient congestus.

CHAPTER 3: AEROSOL BREEZES FROM MESOSCALE AEROSOL GRADIENTS DRIVE PRECIPITATION INCREASES[2]

3.1 Introduction

Large-scale changes in aerosol concentrations have long been understood to be associated with changes in the surface energy budget, cloudiness, and precipitation (Boucher et al. 2013; Kiehl and Briegleb 1993; Kim et al. 2014; Ramanathan et al. 2005). Aerosol particles influence the amount of energy reaching the surface directly via the extinction of incoming solar radiation (McCormick and Ludwig 1967; Atwater 1970), as well as indirectly via microphysical interactions with clouds (Twomey 1977; Tao et al. 2012). These changes subsequently impact surface fluxes, atmospheric warming, and eventually precipitation, with potentially large climatic and societal impacts (Boucher et al. 2013; Tao et al. 2012).

The spatial distribution of aerosol concentrations is also known to be important. On a global scale, the gradient in the aerosol radiative effect between the northern and southern hemispheres influences the location of the ITCZ and its associated precipitation maximum (Allen et al. 2015; Haywood et al. 2013). On a regional scale, changes to monsoon circulations and precipitation have similarly been attributed to gradients in aerosol emissions and their direct effects in areas such as East ,South, and Southeast Asia (Herbert et al. 2021; Hodzic and Duvel 2018; Kim et al. 2016; Lau et al. 2008; Wang et al. 2009).

On smaller scales, variability in horizontal aerosol concentrations on the order of 40-400km has frequently been observed in concert with major aerosol sources, sinks, and transport

[2] This study, titled "'Aerosol Breezes' from Mesoscale Aerosol Gradients Drive Precipitation Increases" (Leung, G.R. and S.C. van den Heever, 2022, in preparation) is in preparation for submission.

pathways (Anderson et al. 2003; Chakraborty et al. 2021; Holben et al. 2018). For example, horizontal aerosol gradients typically exist on the edges wildfire smoke plumes (Kelleher et al. 2018; Palm et al. 2021) or urban areas (Lin et al. 2021; Pierce et al. 2019). However, relatively little work has been done linking those mesoscale aerosol gradients to cloud or precipitation feedbacks.

Mesoscale variations in surface fluxes due to contrasts in surface properties (e.g. sea breeze, forest breeze, slope flows) are known to drive thermal circulations that are important for organizing and enhancing cloudiness and precipitation (Argüeso et al., 2016; Cronin et al., 2015; Garcia-Carreras et al., 2011; Park et al. 2020). Furthermore, in the tropics where synoptic pressure gradients are generally weak, mesoscale pressure gradients due to differential heating play a strong role in defining wind patterns and convection (Nesbitt and Zipser 2003; Qian 2008; Yang and Slingo 2001). Horizontally-uniform changes to aerosol concentrations are also known to impact the strength of mesoscale circulations by influencing incoming solar radiation (Grant & Heever, 2014; Park & van den Heever, 2022). It is thus conceivable that mesoscale horizontal gradients in aerosol concentration over an otherwise uniform surface may drive thermal circulations similar to sea breezes, thereby enhancing cloudiness and precipitation. We will refer to such aerosol gradient-induced circulations as “aerosol breezes”.

Lee et al. (2014) confirmed that spatial gradients in absorbing aerosol concentration could generate circulation patterns influencing cloud formation, both by reducing the amount of radiation reaching the surface and by changing the static stability of the boundary layer. These two effects act in opposite directions, with the net impact on the circulation depending on the location and magnitude of the gradient. We expect aerosol particles which are primarily scattering (e.g. sulfates) may similarly increase extinction, but would have relatively minor

changes to the static stability of the atmosphere. Thus, the impacts of spatial gradients in scattering aerosol concentration on convection may be even more pronounced.

In this paper, we study the impacts of mesoscale horizontal variability in sulfate aerosol concentrations on the frequency, distribution and precipitation amounts of shallow convective clouds. Our goal is to determine whether mesoscale gradients in sulfate aerosol can drive aerosol breezes, and if so, what the subsequent impacts of aerosol breezes are on clouds and precipitation. We also aim to assess the implications and potential biases introduced by failing to resolve these mesoscale aerosol gradients in larger-scale regional and climate models. Given that aerosol breezes are likely to become increasingly important as wildfire risk continues to increase with changing climates (Diffenbaugh et al. 2021), and the spatial pattern of urban/industrial emissions shift due to both increased emission controls and rapid urbanization in different parts of the world (Collaud Coen et al. 2020), it is important that we understand and appropriately forecast such effects.

3.2 Model description and configuration

We used the Regional Atmospheric Modeling System (RAMS, version 6.3.02) to run the simulations in this study (Cotton et al. 2003; Saleeby and van den Heever 2013). RAMS is a non-hydrostatic atmospheric model with a sophisticated two-moment bin-emulating bulk microphysics scheme; full representation of aerosol sources, sinks, and advection; coupled surface fluxes using the LEAF-3 submodel; and an interactive two-stream radiation scheme including aerosol-radiative effects. Further details about the model set-up can be found in **Table 3.1** and associated references.

Our model grid spanned 100x100km horizontally—similar in size to a single 1x1º GCM grid box—at a horizontal spatial resolution of 100m. In the vertical direction, the model grid was

20km tall, with spacing stretching between 50 and 300m to resolve the cumulus cloud field and boundary layer processes. The simulation is highly idealized, but broadly intended to represent summer monsoon conditions in the Maritime Continent. Initial conditions were based on the mean ERA-5 profile over a 2x2º box over Luzon Island of the Philippines during September 2019 to coincide with the Cloud, Aerosol, and Monsoon Process Philippines Experiment ($CAMP^2Ex$) (**Figure 3.1a-b**).

The initial aerosol gradient followed a sine curve meridionally, such that aerosol concentration was maximized in the center of the domain and fell off smoothly towards the domain edges (**Figure 3.1b**). Aerosol concentrations were zonally uniform and decreased exponentially in the vertical (**Figure 3.1d**). The model set-up therefore represents aerosol gradients that might be observed surrounding a smoke plume, an urban region, or other mesoscale aerosol sources. This run is referred to as the *Gradient* run. For comparison, we also ran a *Control* simulation with an integrated aerosol mass and number equal to the *Gradient* run but distributed homogenously in the horizontal (**Figure 3.1c**). In both simulations, the aerosol gradient was maintained via a source function identical to the initial aerosol concentrations in the respective simulations over the first 1 km AGL, with the initial aerosol concentration replenished on the timescale of a day. To test the sensitivity of the results to the magnitude of aerosol concentrations, we performed an additional set (*Gradient* and *Control* runs) of simulations with reduced aerosol concentrations (**Figure 3.2**). We primarily present results from the initial set of simulations, but where relevant, we refer to these set of sensitivity tests as "reduced" runs (i.e. *Reduced-Gradient* and *Reduced-Control* as opposed to the *Gradient* and *Control* runs).

After initialization, the simulation was allowed to evolve without additional large-scale forcing except the aerosol emissions. The diurnal cycle was not represented, and the sun was set at a constant solar zenith equivalent to local solar noon.

To count and compare the number of updrafts in different regions of the domain, we used the *tobac* (Tracking and Object-Based Analysis of Clouds, version 1.4) algorithm, which can identify and track updrafts through time (Heikenfeld et al., 2019; Sokolowsky et al., 2022). The updraft features are first identified in three-dimensions as relative maxima in vertical velocities above multiple threshold values (1, 3, 5 m s^{-1}). These updrafts are then linked in time by matching features in previous timesteps based on the predicted updraft motion. We excluded any features that had a lifetime of less than 5 minutes (i.e. the feature had to be identified in at least two consecutive output files).

3.3 Induced aerosol breeze circulation and precipitation response

Within 4 hours from initialization, a distinct circulation forms between the low- and high-aerosol regions of the domain. **Figure 3.2** depicts the mean cloud condensate, downwelling shortwave radiation, and wind fields, temporally and zonally averaged as a function of altitude and distance from the maximum aerosol concentration (i.e. averaged by the distance from the center of the domain as denoted by the black line in **Figure 3.1b**).

Aerosol optical depth (**Figure 3.2c**) is highest in the center of the domain, in line with the prescribed aerosol gradient. As a result of the increased light extinction, the downwelling shortwave at the surface is ~30 W m^2 lower at the center than at the edges of the domain where aerosol concentrations are lowest (**Figure 3.2b**). This leads to uneven heating of the land surface and a gradient in surface heat fluxes that is opposite in direction to the gradient in aerosol concentration (**Figure 3.2d**). This drives a pressure gradient and net wind flow directed from the

high- to low-aerosol region at altitudes between the surface and the top of the surface-based mixed layer/cloud base (**Figure 3.2a,b**). Above those altitudes, there is a compensating return flow aloft up to ~2km. Although there is still a difference in the downwelling shortwave flux above those altitudes (**Figure 3.2b**), the height of the return flow is limited by the increase in static stability (**Figure 3.1a**) at the tropical trade wind inversion (~2km AGL). Low-level convergence favors rising motion over the low-aerosol region, and subsiding motion over the high-aerosol region (**Figure 3.2a**).The aerosol-induced circulation that develops is thus an aerosol breeze, and is similar to other thermally-driven mesoscale circulations such as sea breezes, both in terms of its driving mechanism and general structure (Antonelli and Rotunno 2007; Garcia-Carreras et al. 2011).

This aerosol-induced circulation leads to the preferential development of clouds and precipitation over the low-aerosol region of the aerosol gradient. **Figure 3.3** depicts the number of raining clouds (**Figure 3.3b**) and accumulated precipitation (**Figure 3.3c**) averaged spatially as in **Figure 3.2**, and demonstrates this uneven distribution of convection and precipitation. Clouds forming over the low-aerosol region have greater coverage, higher cloud tops (**Figure 3.2**), and are more likely to produce rain (**Figure 3.3c**) compared to clouds over the high-aerosol region of the gradient. Almost none of the rain falls over the high-aerosol region, instead being concentrated over the low-aerosol region.

Relative to the *Control*, the additional low-level convergence driven by the aerosol gradient increases the number of precipitating clouds (**Figure 3.3b**) and the total amount of accumulated precipitation (**Figure 3.3c**) produced within the domain. The onset of rain also occurs an hour sooner in the presence of a strong aerosol gradient relative to *Control* (**Figure 3.4**), with the difference in domain-wide accumulated precipitation between the two simulations

being ~25% after 12 hours (**Figure 3.4b**). This demonstrates that the aerosol breeze is further analogous to other mesoscale flows driven by surface heterogeneities in its capacity not only to redistribute convection throughout the domain, but also to actually increase it.

Studies examining the interactions between aerosols and clouds often do not realistically represent the spatial heterogeneity in aerosol gradients. Thus, their estimated aerosol-cloud-precipitation interactions may not accurately reflect the magnitude of such effects in regions of strong aerosol gradients. Furthermore, this result suggests that unrepresented aerosol heterogeneities across typical climate and regional model grid cells may lead to biases in rain timing, distribution, and even total amount.

3.4 Sensitivity to aerosol loading

We additionally tested the sensitivity of the idealized aerosol breeze circulation to the magnitude of the aerosol loading by conducting a set of *Reduced* simulations with half the aerosol loading as in the initial simulations. A qualitatively similar circulation develops under the *Reduced-Gradient* simulations (not shown), though the magnitude of the gradient in surface fluxes is reduced in proportion to the reductions in the AOD contrast between low- and high-aerosol portions of the domain (**Figure 3.2c,d**). However, the increase in convection associated with the aerosol breeze is sensitive to the magnitude of the aerosol gradient. Although an aerosol breeze does develop and subsequently increases clouds and precipitation in the low-aerosol region (**Figure 3.3a-c**) of the *Reduced-Gradient* simulation, a much smaller change in the total amount of precipitation is produced relative to the *Reduced-Control* simulation (**Figure 3.4a,b**). This suggests the net impact of the aerosol gradient on accumulated precipitation results from the competition between direct (i.e. reduction in radiation over high-aerosol regions) (Kim et al.

2014; McCormick and Ludwig 1967; Atwater 1970) and indirect (i.e. microphysical invigoration of warm clouds over high-aerosol regions) (Twomey 1977; Tao et al. 2012) effects.

3.5 Observational case studies

Although we tested the concept of an aerosol breeze in an idealized modeling scenario, we expect similar aerosol gradients and associated circulations and cloud processes in regions of actual localized aerosol emissions such as wildfires, urban areas, industrial zones, and volcanic plumes. Two examples of such cases are demonstrated in **Figure 3.5**.

The first case shown in **Figure 3.5a,b** involves a likely aerosol breeze over Kentucky and central Tennessee, USA on 3 July, 2021 associated with wildfire smoke advecting into the region. The wildfire smoke formed a strong aerosol gradient between the regions labelled "high-aerosol" and "low-aerosol". AODs ranged between <0.01 in the low-aerosol region to ~0.5 in the high-aerosol region over an area of a few hundred kilometers. Throughout the day, shallow cumulus clouds developed in the low-aerosol region.

The second case is presented in **Figure 3.5c**, and shows an image captured from the International Space Station over southwestern Australia on 12 January 2020. A smoke plume from an active fire is located in the center of the image, with smoke being advected to the east/southeast over a distance on the order of a 100km. Along the northeast corner of the image, a field of shallow clouds developed only in the clear-air or low aerosol region along the edges of the smoke plume.

These two observational cases are certainly more complex than the idealized modeling case we presented earlier. The smoke in **Figure 3.5a,b** was transported far enough away from the fire source that it produces an aerosol gradient along a straight line similar to our idealized simulation. However, we would expect aerosol plumes to be more conical closer to a point

source, as in **Figure 3.5c**; this would lead to aerosol gradients both parallel and perpendicular to the direction of plume advection, which might impact the aerosol breeze circulation. That being said, both observational cases are remarkably similar in spatial scale, aerosol gradient set-up, and cloud formation to the idealized modeling case we presented in Section 2.3. These cases thus lend credibility to the notion that the impact of localized aerosol emissions on mesoscale phenomena as a result of the direct aerosol effect is important and should be considered.

3.6 Discussion and conclusions

To examine the capacity of horizontal aerosol gradients to drive mesoscale circulations and convection, we conducted a set of high-resolution RAMS simulations. We found that a horizontal gradient in scattering aerosol concentrations produced an "aerosol breeze", similar to other mesoscale phenomena driven by gradients in surface fluxes, such as sea breezes or urban flows.

The aerosol breeze in our idealized simulations resulted in shifts in the spatial distribution of clouds and precipitation. Relative to a *Control* simulation without an aerosol gradient, but with the same integrated aerosol mass and number, the *Gradient* simulation produced more clouds, initiated precipitation sooner, and generated more rainfall. We show that mesoscale aerosol gradients similar to those presented here, which might be expected around thick wildfire plumes, can be important controls on the number of shallow convective clouds (i.e. cumulus, congestus) and the precipitation they produce. Even reduced gradients in aerosol loading can be crucial for the distribution and timing of clouds and precipitation.

These results demonstrate that even in the absence of other mesoscale heterogeneities in surface properties, a sufficiently strong gradient in aerosol concentrations alone can drive an aerosol breeze that impacts the mesoscale circulation and cloud properties. Additionally, these

results suggest that failing to represent the radiative impacts and resulting circulations induced by mesoscale (and hence sub-grid scale) horizontal aerosol gradients on the order of the size of a single GCM grid cell, may lead to significant biases in the predicted timing and amounts of cloudiness and precipitation within GCM and regional models. Impacts from unrepresented aerosol gradients may also confound the estimation of aerosol-cloud-precipitation feedbacks in other higher-resolution studies which do not appropriately represent the spatial heterogeneity of aerosol emissions. Finally, we showed two observational cases associated with the advection of thick wildfire smoke that appear to support the aerosol breeze phenomenon identified in our idealized modeling simulations.

The results presented here serve as an upper bounding case to demonstrate the primary physical processes involved in producing the aerosol breeze. Our findings emphasize the need for greater consideration of aerosol breezes in future work, particularly in investigating the sensitivity of aerosol breezes to meteorology, aerosol type, land surface, varied spatial distributions, and interactions with other circulations (such as sea breezes or buoyant firestorm plumes). Such research is particularly essential given projected changes globally to the spatial distribution of aerosol emissions in urban and industrial areas, as well as in wildfires, with changing climates.

3.7 Tables

Table 3.1. RAMS model options used in simulation.

Model Aspect	**Setting**
Grid	Arakawa C grid
	1000 x 1000 points, $\Delta x = \Delta y = 100m$
	120 vertical levels, $\Delta z = 50 - 300\ m$
Time integration	12 hour simulation duration, $\Delta t = 1s$
	Output analysis files every 5 minutes

Initialization	Horizontally homogenous thermodynamic profile, averaged from ERA-5 as described in text
	No initial background winds
	Random potential temperature perturbations within the lowest 500m AGL of the domain, with a maximum perturbation of 0.1K
Surface scheme	Uniform surface of evergreen broadleaf tree and silty clay loam soil
	LEAF-3 (Walko et al. 2000)
Boundary conditions	Periodic in zonal and meridional directions
Microphysics scheme	Two-moment bulk microphysics (Meyers et al. 1997)
	8 hydrometeor classes (Saleeby and Cotton 2004)
Radiation scheme	Two-stream, hydrometeor sensitive (Harrington 1997)
	Updated every 1 minute
Aerosol treatment	Ammonium sulfate aerosol, with single log-normal mode (Saleeby and van den Heever 2013)
	Varying concentration in the horizontal as depicted in Figure 3.1c
	Maximum concentration at the surface and exponentially decreasing with altitude
	Aerosol-radiation interactions on
	Aerosol sources and sinks on, with full aerosol budget tracking (Saleeby & van den Heever, 2013)

3.8 Figures

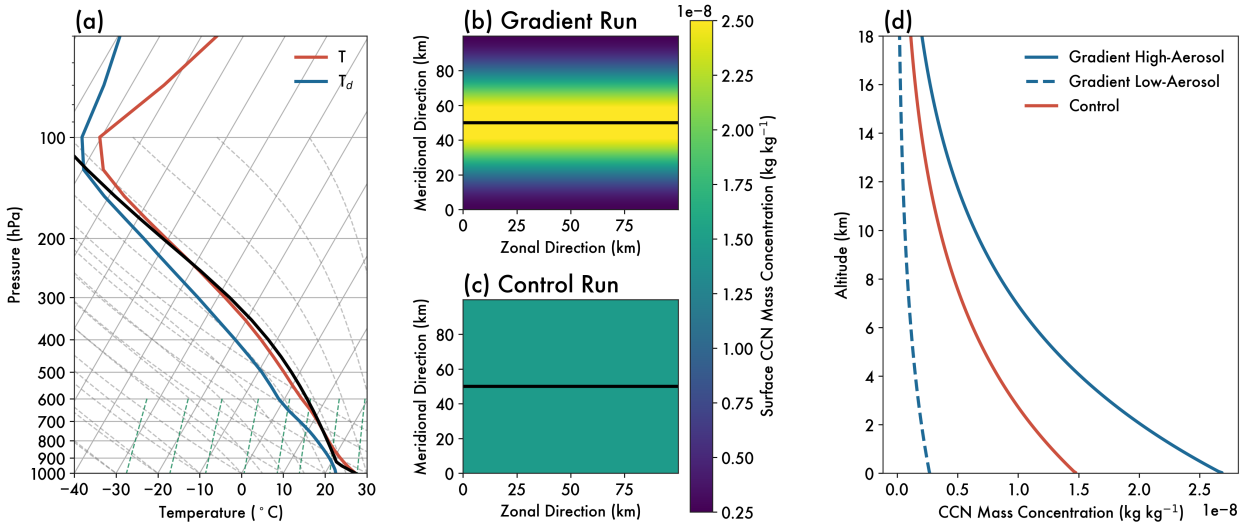

Figure 3.1. Model set-up details. (a) Skew*T* – log*p* diagram showing the sounding used to initialize the numerical simulation. The black line is a parcel trajectory from the surface. Plan view of the surface aerosol mass concentration are shown for the (b) *Gradient* run and (c) *Control* run. The black horizontal line in (b) and (c) indicates the center of the domain and aerosol gradient (peak aerosol loading), as described in text. (d) Vertical profile of aerosol mass concentration for the *Control* run (red line), and high- (blue solid line) and low-aerosol (blue dashed line) regions of the *Gradient* run.

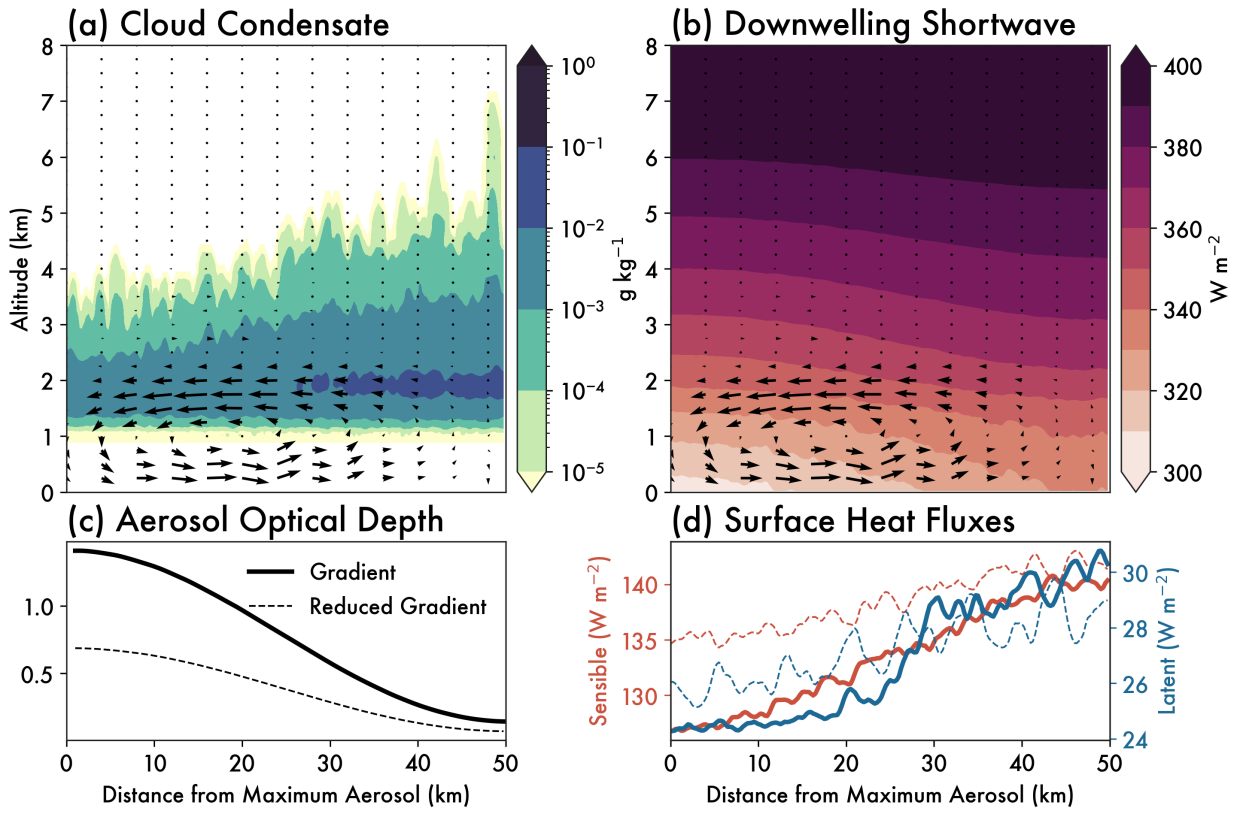

Figure 3.2. Mean cross section through the *Gradient* domain over all 12 hours of the simulation, averaged temporally and zonally. The abscissa is given as a function of distance from the domain center/maximum aerosol concentration (horizontal black line in Figure 3.1b,c), such that the high-aerosol region is on the left and the low-aerosol region is on the right of these panels. Shading in (a) shows cloud condensate mixing ratios (g kg^{-1}), and in (b) the downwelling shortwave flux (W m^{-2}). The wind barbs in (a) and (b) show the mean vertical and horizontal winds perpendicular to the black line in Figure 3.1b,c. The aerosol optical depth at the surface is represented in (c), while (d) depicts the sensible surface heat flux in red (left y-axis; W m^{-2}) and latent surface heat flux in blue (right y-axis; W m^{-2}), all averaged temporally and zonally. The dashed lines in (c,d) show the same quantities for the *Reduced-Gradient* simulation.

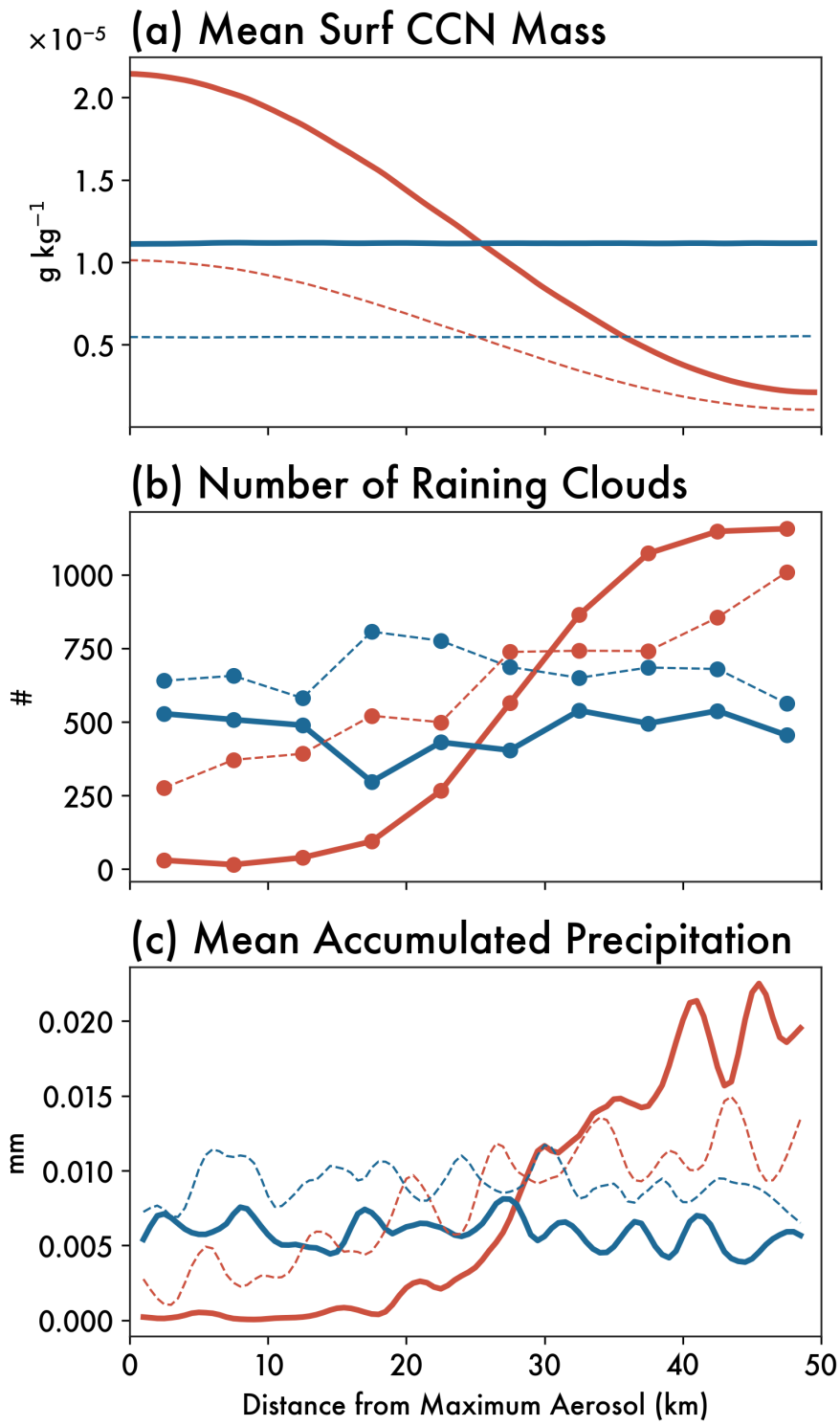

Figure 3.3. Comparison of *Gradient* (red) and *Control* (blue) simulations in terms of (a) mean surface aerosol mass concentration (g kg^{-1}), (b) number of clouds with mean precipitation rates of at least 0.1 mm hr^{-1}, and (c) mean accumulated precipitation per grid cell (mm). The dashed lines in both panels show the same quantities for the *Reduced-Gradient* and *Reduced-Control* simulations.

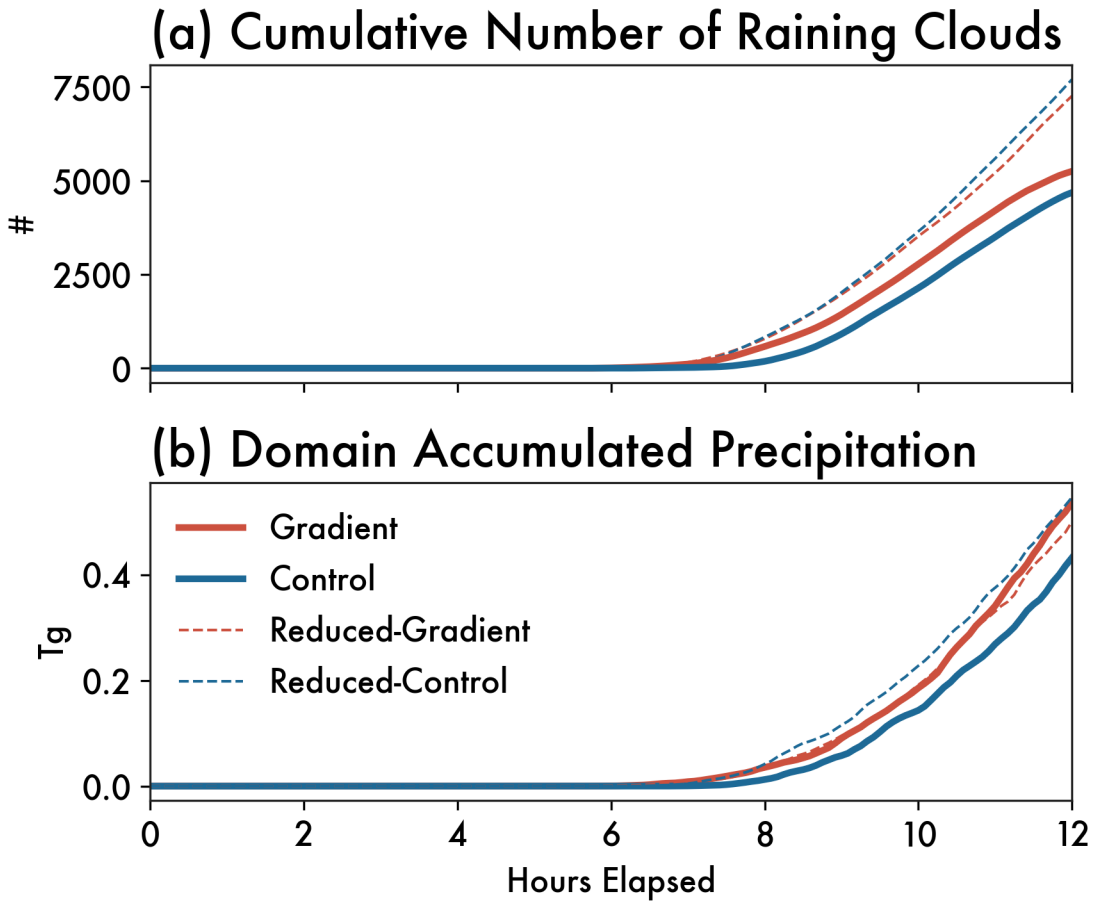

Figure 3.4. Timeseries comparisons of the *Gradient* (red) and *Control* (blue) simulations in terms of (a) cumulative number of raining clouds (mean rain rate of at least 0.1 mm hr^{-1}), and (b) total domain accumulated precipitation (Tg) over the 12 hours of the simulation. The dashed lines in both panels show the same quantities for the *Reduced-Gradient* and *Reduced-Control* simulations.

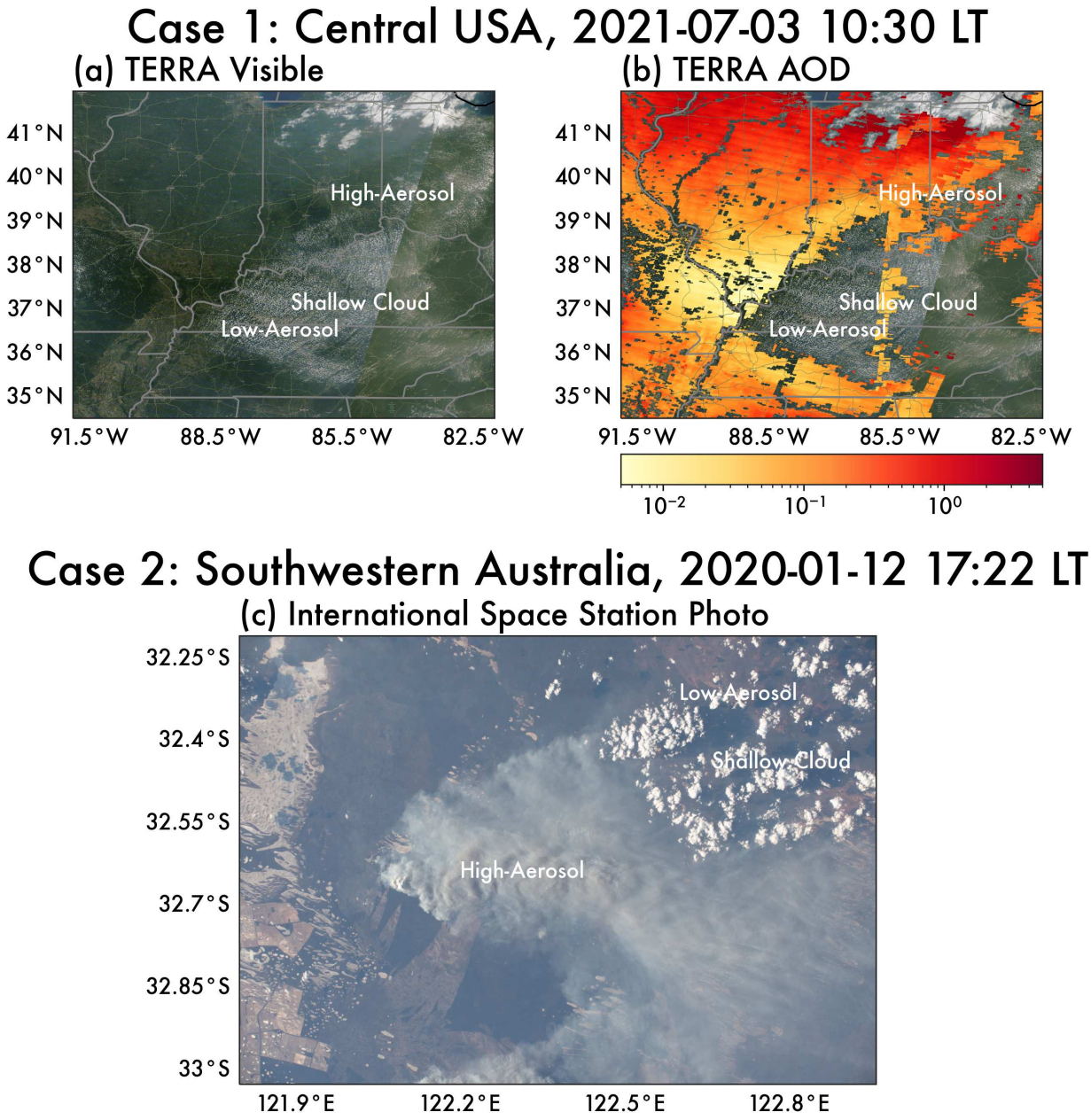

Figure 3.5. Two observational examples of a strong aerosol gradient with associated shallow cumulus formation. The top row (a,b) shows smoke advection over Kentucky and central Tennessee, USA on 3 July 2021. (a) Visible channel and (b) aerosol optical depth (3km resolution) from TERRA. Note that black regions in (b) are areas where no AOD was retrieved due to cloud cover. The bottom row (c) shows smoke advection over southwestern Australia on 12 January 2020. The image was captured from the International Space Station (image ID: ISS061-E-123446, accessed from eol.jsc.nasa.gov courtesy of the Earth Science and Remote Sensing Unit, NASA Johnson Space Center). Regions of high- and low-aerosol, as well as shallow cloud cover are annotated.

CHAPTER 4: CONCLUSIONS

4.1 Summary and implications of key findings

Given that shallow clouds are ubiquitous and very crucial for the climate system, there has already been much research devoted to improving our understanding of them. That being said, there are also many remaining aspects of their development which remain understudied. Thus, the overarching goal of this thesis was to investigate the mechanisms driving differences in shallow convective cloud development and their interactions with the aerosol environment. We were able to address this goal by conducting idealized high-resolution LES and utilizing newly-developed tracking and compositing techniques.

In Chapter 2, we explored the factors controlling the development of congestus clouds relative to the 0ºC stable layer, and the implications of that development on the transport of aerosols and water vapor into the midlevels. We identified, tracked, and composited over a thousand tropical congestus updrafts and their near-environments, and drew the following conclusions:

1. Terminal congestus (i.e. those which are vertically capped by the 0ºC stable layer) and transient congestus (i.e. those which can develop vertically above the 0ºC stable layer) have similar structures: both consist of an overturning circulation between a core updraft and a relatively weak subsiding shell. However, terminal congestus downdrafts are more vertically homogenous and extend all the way to cloud base. Transient congestus updrafts, on the other hand, have stronger maxima above the 0ºC level, and their overturning circulations are broken into distinct branches separated by the 0ºC and trade wind stable layers.

2. Buoyancy between the 0ºC and trade wind stable layers is the primary factor differentiating terminal and transient congestus. The differences in buoyancy are driven by transient congestus being surrounded by more humid mid-level environments, which better protects them from evaporation and maintains stronger updrafts near and at the 0ºC level.
3. Terminal congestus tend to detrain more aerosol back into the environment along the edges of the updraft as a result of increased evaporation. On the other hand, transient congestus have a stronger impact on their environments beyond the subsiding shell, since they detrain aerosols and water vapor above the 0ºC level which are vertically trapped by the stable layer and radially transported to form mid-level aerosol layers.

While terminal and transient congestus have similar structures, these results demonstrate our understanding of the environments that might be more favorable to congestus development. Furthermore, they show that the ratio of terminal to transient congestus within an environment has implications for the location and development of mid-level aerosol layers. The aerosol particles detrained from congestus represent a proportionally large increase in mid-level aerosol, relative to background conditions. Thus, the mechanisms we described demonstrate one potential pathway (in addition to other pathways such as new particle formation in the free troposphere) for aerosol particles to be transported to the mid-troposphere for interactions with deeper cloud systems or mid-level clouds such as altocumulus.

In Chapter 3, we examined the impacts of mesoscale horizontal gradients in aerosol concentrations—as might be expected around wildfire plumes or at the edges of urban areas—on the development and distribution of shallow convective clouds. We present an observational example of such a case, and we use an idealized LES to show that:

1. A mesoscale gradient in aerosol concentrations spanning 100km horizontally can drive "aerosol breeze" circulations due to the difference in incoming radiation across the gradient. These circulations are similar to other mesoscale phenomena driven by surface flux heterogeneities, like sea breezes.
2. Strong horizontal gradients in aerosol emissions cause sooner and more intense precipitation than the same amount of integrated aerosol mass uniformly distributed in the horizontal. Although the same circulation develops under reduced aerosol loadings, the net changes in precipitation are dependent on the competition between direct radiative feedbacks responsible for shutting down the initiation of shallow convection and the indirect effect of warm-phase invigoration, both of which are ultimately dependent on the magnitude of aerosol loading.
3. Unrepresented sub-grid scale heterogeneity in horizontal aerosol distributions may lead to biases in the distribution, timing, and amounts of simulated clouds and precipitation.

Although it is fairly well understood that the horizontal distribution of aerosols is important on a mean global and regional scale, the results of this study underscore their importance in driving mesoscale circulations. Aerosol breezes are likely to play an important role in distributions of convection and precipitation around areas of highly-localized emissions. As urban and industrial emission patterns shift and the risk of large wildfires increases, it becomes even more critical to characterize these circulations.

4.2 Future work

The findings presented in this thesis have contributed to fundamental descriptions of the controls on shallow cloud development and their interactions with the aerosol environment. By breaking down more complicated observed phenomena, such as mid-level aerosol detrainment

layers and strong gradients in aerosol concentration, into simple but testable idealized modelling experiments, we have been able to describe some of the primary driving mechanisms behind these convective processes. At the same time though, many new questions have been raised by this research.

Firstly, while the simulations we conducted for both Chapter 2 and 3 are fairly idealized and therefore have general applicability, they are both based on observations made during the CAMP^{2}Ex field campaign. It would thus be interesting to examine how these findings are influenced by a variety of other thermodynamic environments in present and future climate scenarios and/or land surface types. In Chapter 2, we showed that there was a clear relationship between the environment (specifically the midlevel moisture) and how much congestus were able to develop; further testing over a broader range of environments will help to identify the sensitivities of this relationship to other parameters. In Chapter 3, we found that the depth aerosol breeze circulation was related to the height of the trade wind inversion—other similar mesoscale circulations such as sea breezes have been shown to have strong dependence on environmental factors such as inversion layer strength, boundary layer height, and initial wind speed (Grant and van den Heever 2014; Igel et al. 2018; Park et al. 2020), and similar analyses might be pursued for the aerosol breeze.

Secondly, we have described the two-way interactions between shallow convection and the aerosol environment, but many of these interactions may have some dependence on aerosol loading and type. We showed in Chapter 2 that the strength of mid-level detrainment layers is related to the proportion of terminal to transient congestus. Previous studies have demonstrated that increased aerosol loadings lead to warm-phase invigoration and a greater proportion of congestus developing above the freezing level (Li et al. 2013b; Sheffield et al. 2015). It would be

valuable to have a better grasp on how increased aerosol loadings might feedback into the transport of aerosol particles into the mid-troposphere, as well as how those feedbacks may vary as a function of aerosol type, which determines the size, hygroscopicity, and radiative properties (i.e. the degree to which they are scattering versus absorbing) of the aerosol particles (Jiang et al. 2018). The use of the *tobac* tracking algorithm in Chapter 2, alongside composites of the near-updraft environment, could be utilized to examine how changes to the aerosol environment impact both terminal and transient congestus.

The analysis framework used in Chapter 2 involving the conditionally-averaged vertical momentum budget also has wider applicability for improving our understanding of uncertainties in model representation of aerosol-cloud interactions. Similar work has been done in Marinescu et al. (2021) to compare how aerosol-deep convective cloud interactions are represented in a variety of models, and would be useful for similar analysis on shallow convective clouds.

We also showed in Chapter 3 that the magnitude and net sign of the precipitation response to aerosol gradients is somewhat sensitive to the aerosol loading. Further analysis into how the magnitude of the direct versus indirect response vary as a function of aerosol loading would help to more precisely identify the ranges of aerosol loading where aerosol breezes may increase precipitation amounts. In addition to this, we expect that other more absorbing aerosols such as black/brown carbon or dust might have different radiative effects and thus a different impact on mesoscale circulations as suggested in Lee et al. (2014).

Finally, comparison to larger-scale, more realistic simulations (Freeman et al., 2022), as well as observations from both satellite and field campaign measurements, would help to assess the generalizability of the processes represented in these idealized simulations. The CloudSat radar has previously been used to identify proportions of terminal to transient congestus (Luo et

al. 2009). This could be extended for a variety of environments, given that the proportion of congestus that develop past the 0ºC stable layer depends on mid-level moisture, as our results in Chapter 2 show. Combining this with other instruments, such as the CALIPSO lidar, to provide vertically-resolved aerosol information might be useful in assessing the real-world impacts of congestus of differing heights on detrained aerosol layers.

The aerosol breeze simulations presented in Chapter 3 are an upper bounding case with relatively high aerosol loading in order to demonstrate the physical processes that lead to the formation of an aerosol breeze. Further simulations with more detailed representations of aerosol gradients (e.g. conical or radial distributions more similar to a plume close to a fire or other point source), simulations incorporating varied present and future meteorology, and simulations including interactions with other mesoscale circulations driven by terrain flows, sea breezes, or land surface heterogeneities would be highly useful to quantify the impacts of the aerosol breeze under a variety of real-world conditions.

More observational examples of the aerosol breeze described in Chapter 3 would also be enlightening. Given advances in high-resolution satellite retrievals of aerosol optical depth (Wei et al. 2018; Lin et al. 2021; Wang et al. 2021), field campaign observations in regions of strong aerosol gradients (such as CAMP^{2}Ex or FIREX-AQ, among many others), and detection of aerosol gradients during transport from reanalysis products (Chakraborty et al. 2021), it seems feasible that aerosol breezes and associated shallow convection could be better characterized in the wide variety of environments found globally. In this way, the physical processes described and highlighted in this work could be further applied to observations.

REFERENCES

Allen, R. J., A. T. Evan, and B. B. B. Booth, 2015: Interhemispheric Aerosol Radiative Forcing and Tropical Precipitation Shifts during the Late Twentieth Century. *Journal of Climate*, **28**, 8219–8246, https://doi.org/10.1175/JCLI-D-15-0148.1.

Anderson, T. L., R. J. Charlson, D. M. Winker, J. A. Ogren, and K. Holmén, 2003: Mesoscale Variations of Tropospheric Aerosols. *Journal of the Atmospheric Sciences*, **60**, 119–136, https://doi.org/10.1175/1520-0469(2003)060<0119:MVOTA>2.0.CO;2.

Antonelli, M., and R. Rotunno, 2007: Large-Eddy Simulation of the Onset of the Sea Breeze. *Journal of the Atmospheric Sciences*, **64**, 4445–4457, https://doi.org/10.1175/2007JAS2261.1.

Argüeso, D., A. Di Luca, and J. P. Evans, 2016: Precipitation over urban areas in the western Maritime Continent using a convection-permitting model. *Clim Dyn*, **47**, 1143–1159, https://doi.org/10.1007/s00382-015-2893-6.

Atwater, M. A., 1970: Planetary Albedo Changes Due to Aerosols. *Science*, **170**, 64–66.

Bony, S., and J.-L. Dufresne, 2005: Marine boundary layer clouds at the heart of tropical cloud feedback uncertainties in climate models. *Geophysical Research Letters*, **32**, https://doi.org/10.1029/2005GL023851.

Boucher, O., and Coauthors, 2013: Clouds and Aerosols. *Climate Change 2013: The Physical Science Basis. Contribution of Working Group I to the Fifth Assessment Report of the Intergovernmental Panel on Climate Change*, Cambridge University Press, 571–658.

Chakraborty, S., B. Guan, D. E. Waliser, A. M. da Silva, S. Uluatam, and P. Hess, 2021: Extending the Atmospheric River Concept to Aerosols: Climate and Air Quality Impacts. *Geophysical Research Letters*, **48**, e2020GL091827, https://doi.org/10.1029/2020GL091827.

Collaud Coen, M., and Coauthors, 2020: Multidecadal trend analysis of in situ aerosol radiative properties around the world. *Atmospheric Chemistry and Physics*, **20**, 8867–8908, https://doi.org/10.5194/acp-20-8867-2020.

Corr, C. A., and Coauthors, 2016: Observational evidence for the convective transport of dust over the Central United States. *Journal of Geophysical Research: Atmospheres*, **121**, 1306–1319, https://doi.org/10.1002/2015JD023789.

Cotton, W. R., and Coauthors, 2003: RAMS 2001: Current status and future directions. *Meteorol Atmos Phys*, **82**, https://doi.org/10.1007/s00703-001-0584-9.

Cotton, W. R., G. H. Bryan, and S. C. Van den Heever, 2011: *Storm and cloud dynamics: the dynamics of clouds and precipitating mesoscale systems*. 2nd ed. Academic Press,.

Cronin, T. W., K. A. Emanuel, and P. Molnar, 2015: Island precipitation enhancement and the diurnal cycle in radiative-convective equilibrium. *Quarterly Journal of the Royal Meteorological Society*, **141**, 1017–1034, https://doi.org/10.1002/qj.2443.

Davies-Jones, R., 2003: An Expression for Effective Buoyancy in Surroundings with Horizontal Density Gradients. *Journal of the Atmospheric Sciences*, **60**, 2922–2925, https://doi.org/10.1175/1520-0469(2003)060<2922:AEFEBI>2.0.CO;2.

Dawe, J. T., and P. H. Austin, 2011: Interpolation of LES Cloud Surfaces for Use in Direct Calculations of Entrainment and Detrainment. *Monthly Weather Review*, **139**, 444–456, https://doi.org/10.1175/2010MWR3473.1.

DeMott, P. J., and Coauthors, 2010: Predicting global atmospheric ice nuclei distributions and their impacts on climate. *Proceedings of the National Academy of Sciences*, **107**, 11217–11222, https://doi.org/10.1073/pnas.0910818107.

Di Girolamo, L., R. E. Holz, J. S. Reid, S. Tanelli, S. C. van den Heever, G. T. Narisma, and J. B. Simpas, 2018: *Cloud and Aerosol Monsoonal Proceses - Philippines Experiment (CAMP2Ex): A proposed joint US-Philippine airborne mission to study aerosol and land use impacts on monsoonal precipitation during late summer 2019*. https://espo.nasa.gov/camp2ex/system/files/group_files/CAMP2Ex-overview-Jul-16-18.pdf (Accessed January 18, 2021).

Diffenbaugh, N. S., A. G. Konings, and C. B. Field, 2021: Atmospheric variability contributes to increasing wildfire weather but not as much as global warming. *Proceedings of the National Academy of Sciences*, **118**, e2117876118, https://doi.org/10.1073/pnas.2117876118.

Drager, A. J., L. D. Grant, and S. C. van den Heever, 2020: Cold Pool Responses to Changes in Soil Moisture. *Journal of Advances in Modeling Earth Systems*, **12**, e2019MS001922, https://doi.org/10.1029/2019MS001922.

Drueke, S., D. J. Kirshbaum, and P. Kollias, 2020: Environmental sensitivities of shallow-cumulus dilution – Part 1: Selected thermodynamic conditions. *Atmos. Chem. Phys.*, **20**, 13217–13239, https://doi.org/10.5194/acp-20-13217-2020.

Engström, A., A. M. L. Ekman, R. Krejci, J. Ström, M. de Reus, and C. Wang, 2008: Observational and modelling evidence of tropical deep convective clouds as a source of mid-tropospheric accumulation mode aerosols. *Geophysical Research Letters*, **35**, https://doi.org/10.1029/2008GL035817.

Fierro, A. O., J. Simpson, M. A. LeMone, J. M. Straka, and B. F. Smull, 2009: On How Hot Towers Fuel the Hadley Cell: An Observational and Modeling Study of Line-Organized Convection in the Equatorial Trough from TOGA COARE. *Journal of the Atmospheric Sciences*, **66**, 2730–2746, https://doi.org/10.1175/2009JAS3017.1.

Freeman, S.W., D.J. Posselt, J.S. Reid, and S.C. van den Heever, 2022: Dynamic and thermodynamic environmental modulation of tropical congestus and cumulonimbus in

the Maritime Continent. Accepted pending revision in *Journal of the Atmospheric Sciences*.

Garcia-Carreras, L., D. J. Parker, and J. H. Marsham, 2011: What is the Mechanism for the Modification of Convective Cloud Distributions by Land Surface–Induced Flows? *Journal of the Atmospheric Sciences*, **68**, 619–634, https://doi.org/10.1175/2010JAS3604.1.

Gentine, P., A. Massmann, B. R. Lintner, S. Hamed Alemohammad, R. Fu, J. K. Green, D. Kennedy, and J. Vilà-Guerau de Arellano, 2019: Land–atmosphere interactions in the tropics – a review. *Hydrology and Earth System Sciences*, **23**, 4171–4197, https://doi.org/10.5194/hess-23-4171-2019.

Grant, L. D., and S. C. van den Heever, 2014: Aerosol-cloud-land surface interactions within tropical sea breeze convection. *Journal of Geophysical Research: Atmospheres*, **119**, 8340–8361, https://doi.org/10.1002/2014JD021912.

——, and S. C. van den Heever, 2014: Aerosol-cloud-land surface interactions within tropical sea breeze convection. *Journal of Geophysical Research: Atmospheres*, **119**, 8340–8361, https://doi.org/10.1002/2014JD021912.

Harrington, J. Y., 1997: Effects of radiative and microphysical processes on simulated warm and transition season Arctic stratus.

Haywood, J. M., A. Jones, N. Bellouin, and D. Stephenson, 2013: Asymmetric forcing from stratospheric aerosols impacts Sahelian rainfall. *Nature Clim Change*, **3**, 660–665, https://doi.org/10.1038/nclimate1857.

van den Heever, S. C., G. L. Stephens, and N. B. Wood, 2011: Aerosol Indirect Effects on Tropical Convection Characteristics under Conditions of Radiative–Convective Equilibrium. *Journal of the Atmospheric Sciences*, **68**, 699–718, https://doi.org/10.1175/2010JAS3603.1.

Heikenfeld, M., P. J. Marinescu, M. Christensen, D. Watson-Parris, F. Senf, S. C. van den Heever, and P. Stier, 2019: tobac 1.2: towards a flexible framework for tracking and analysis of clouds in diverse datasets. *Geosci. Model Dev.*, **12**, 4551–4570, https://doi.org/10.5194/gmd-12-4551-2019.

Herbert, R., P. Stier, and G. Dagan, 2021: Isolating Large-Scale Smoke Impacts on Cloud and Precipitation Processes Over the Amazon With Convection Permitting Resolution. *Journal of Geophysical Research: Atmospheres*, **126**, e2021JD034615, https://doi.org/10.1029/2021JD034615.

Hernandez-Deckers, D., and S. C. Sherwood, 2016: A Numerical Investigation of Cumulus Thermals. *Journal of the Atmospheric Sciences*, **73**, 4117–4136, https://doi.org/10.1175/JAS-D-15-0385.1.

Heus, T., and H. J. J. Jonker, 2008: Subsiding Shells around Shallow Cumulus Clouds. *Journal of the Atmospheric Sciences*, **65**, 1003–1018, https://doi.org/10.1175/2007JAS2322.1.

——, ——, H. E. A. Van den Akker, E. J. Griffith, M. Koutek, and F. H. Post, 2009: A statistical approach to the life cycle analysis of cumulus clouds selected in a virtual reality environment. *Journal of Geophysical Research: Atmospheres*, **114**, https://doi.org/10.1029/2008JD010917.

Hodzic, A., and J. P. Duvel, 2018: Impact of Biomass Burning Aerosols on the Diurnal Cycle of Convective Clouds and Precipitation Over a Tropical Island. *Journal of Geophysical Research: Atmospheres*, **123**, 1017–1036, https://doi.org/10.1002/2017JD027521.

Holben, B. N., and Coauthors, 2018: An overview of mesoscale aerosol processes, comparisons, and validation studies from DRAGON networks. *Atmos. Chem. Phys.*, **18**, 655–671, https://doi.org/10.5194/acp-18-655-2018.

Igel, A. L., and S. C. van den Heever, 2021: Invigoration or Enervation of Convective Clouds by Aerosols? *Geophysical Research Letters*, **48**, e2021GL093804, https://doi.org/10.1029/2021GL093804.

——, ——, and J. S. Johnson, 2018: Meteorological and Land Surface Properties Impacting Sea Breeze Extent and Aerosol Distribution in a Dry Environment: Factors Impacting Sea Breezes. *J. Geophys. Res. Atmos.*, **123**, 22–37, https://doi.org/10.1002/2017JD027339.

Jensen, M. P., and A. D. Del Genio, 2006: Factors Limiting Convective Cloud-Top Height at the ARM Nauru Island Climate Research Facility. *Journal of Climate*, **19**, 2105–2117, https://doi.org/10.1175/JCLI3722.1.

Jiang, H., and G. Feingold, 2006: Effect of aerosol on warm convective clouds: Aerosol-cloud-surface flux feedbacks in a new coupled large eddy model. *Journal of Geophysical Research: Atmospheres*, **111**, https://doi.org/10.1029/2005JD006138.

Jiang, J. H., H. Su, L. Huang, Y. Wang, S. Massie, B. Zhao, A. Omar, and Z. Wang, 2018: Contrasting effects on deep convective clouds by different types of aerosols. *Nat Commun*, **9**, 3874, https://doi.org/10.1038/s41467-018-06280-4.

Johnson, R. H., T. M. Rickenbach, S. A. Rutledge, P. E. Ciesielski, and W. H. Schubert, 1999: Trimodal Characteristics of Tropical Convection. *JOURNAL OF CLIMATE*, **12**, 22.

Kelleher, S., C. Quinn, D. Miller-Lionberg, and J. Volckens, 2018: A low-cost particulate matter ($PM_{2.5}$) monitor for wildland fire smoke. *Atmospheric Measurement Techniques*, **11**, 1087–1097, https://doi.org/10.5194/amt-11-1087-2018.

Kiehl, J. T., and B. P. Briegleb, 1993: The Relative Roles of Sulfate Aerosols and Greenhouse Gases in Climate Forcing. *Science*, **260**, 311–314.

Kim, D., C. Wang, A. M. L. Ekman, M. C. Barth, and D.-I. Lee, 2014: The responses of cloudiness to the direct radiative effect of sulfate and carbonaceous aerosols. *Journal of*

Geophysical Research: Atmospheres, **119**, 1172–1185, https://doi.org/10.1002/2013JD020529.

Kim, M. J., S.-W. Yeh, and R. J. Park, 2016: Effects of sulfate aerosol forcing on East Asian summer monsoon for 1985–2010. *Geophysical Research Letters*, **43**, 1364–1372, https://doi.org/10.1002/2015GL067124.

Kuang, Z., and C. S. Bretherton, 2006: A Mass-Flux Scheme View of a High-Resolution Simulation of a Transition from Shallow to Deep Cumulus Convection. *Journal of the Atmospheric Sciences*, **63**, 1895–1909, https://doi.org/10.1175/JAS3723.1.

Lau, K. M., and H. T. Wu, 2003: Warm rain processes over tropical oceans and climate implications. *Geophysical Research Letters*, **30**, https://doi.org/10.1029/2003GL018567.

Lau, K.-M., and Coauthors, 2008: The Joint Aerosol–Monsoon Experiment: A New Challenge for Monsoon Climate Research. *Bulletin of the American Meteorological Society*, **89**, 369–384, https://doi.org/10.1175/BAMS-89-3-369.

Lee, S. S., G. Feingold, A. McComiskey, T. Yamaguchi, I. Koren, J. V. Martins, and H. Yu, 2014: Effect of gradients in biomass burning aerosol on shallow cumulus convective circulations. *Journal of Geophysical Research: Atmospheres*, **119**, 9948–9964, https://doi.org/10.1002/2014JD021819.

Li, X., W.-K. Tao, H. Masunaga, G. Gu, and X. Zeng, 2013a: Aerosol Effects on Cumulus Congestus Population over the Tropical Pacific: A Cloud-Resolving Modeling Study. *Journal of the Meteorological Society of Japan*, **91**, 817–833, https://doi.org/10.2151/jmsj.2013-607.

——, ——, ——, ——, and ——, 2013b: Aerosol Effects on Cumulus Congestus Population over the Tropical Pacific: A Cloud-Resolving Modeling Study. *Journal of the Meteorological Society of Japan*, **91**, 817–833, https://doi.org/10.2151/jmsj.2013-607.

Lin, H., S. Li, J. Xing, T. He, J. Yang, and Q. Wang, 2021: High resolution aerosol optical depth retrieval over urban areas from Landsat-8 OLI images. *Atmospheric Environment*, **261**, 118591, https://doi.org/10.1016/j.atmosenv.2021.118591.

Luo, Z., G. Y. Liu, G. L. Stephens, and R. H. Johnson, 2009: Terminal versus transient cumulus congestus: A CloudSat perspective. *Geophysical Research Letters*, **36**, https://doi.org/10.1029/2008GL036927.

Malkus, J. S., 1952: Recent Advances in the Study of Convective Clouds and their Interaction with the Environment1. *Tellus*, **4**, 71–87, https://doi.org/10.1111/j.2153-3490.1952.tb00992.x.

Mapes, B., S. Tulich, J. Lin, and P. Zuidema, 2006: The mesoscale convection life cycle: Building block or prototype for large-scale tropical waves? *Dynamics of Atmospheres and Oceans*, **42**, 3–29, https://doi.org/10.1016/j.dynatmoce.2006.03.003.

Marinescu, P. J., and Coauthors, 2021: Impacts of Varying Concentrations of Cloud Condensation Nuclei on Deep Convective Cloud Updrafts—A Multimodel Assessment. *Journal of the Atmospheric Sciences*, **78**, 1147–1172, https://doi.org/10.1175/JAS-D-20-0200.1.

Masunaga, H., T. S. L'Ecuyer, and C. D. Kummerow, 2005: Variability in the Characteristics of Precipitation Systems in the Tropical Pacific. Part I: Spatial Structure. *Journal of Climate*, **18**, 823–840, https://doi.org/10.1175/JCLI-3304.1.

McCormick, R. A., and J. H. Ludwig, 1967: Climate Modification by Atmospheric Aerosols. *Science*, **156**, 1358–1359, https://doi.org/10.1126/science.156.3780.1358.

McGee, C. J., and S. C. van den Heever, 2014: Latent Heating and Mixing due to Entrainment in Tropical Deep Convection. *Journal of the Atmospheric Sciences*, **71**, 816–832, https://doi.org/10.1175/JAS-D-13-0140.1.

Mecikalski, J. R., C. P. Jewett, J. M. Apke, and L. D. Carey, 2016: Analysis of Cumulus Cloud Updrafts as Observed with 1-Min Resolution Super Rapid Scan GOES Imagery. *Monthly Weather Review*, **144**, 811–830, https://doi.org/10.1175/MWR-D-14-00399.1.

Medeiros, B., B. Stevens, and S. Bony, 2015: Using aquaplanets to understand the robust responses of comprehensive climate models to forcing. *Clim Dyn*, **44**, 1957–1977, https://doi.org/10.1007/s00382-014-2138-0.

Meyers, M. P., R. L. Walko, J. Y. Harrington, and W. R. Cotton, 1997: New RAMS cloud microphysics parameterization. Part II: The two-moment scheme. *Atmospheric Research*, **45**, 3–39, https://doi.org/10.1016/S0169-8095(97)00018-5.

Morrison, H., and J. M. Peters, 2018: Theoretical Expressions for the Ascent Rate of Moist Deep Convective Thermals. *Journal of the Atmospheric Sciences*, **75**, 1699–1719, https://doi.org/10.1175/JAS-D-17-0295.1.

——, ——, A. C. Varble, W. M. Hannah, and S. E. Giangrande, 2020: Thermal Chains and Entrainment in Cumulus Updrafts. Part I: Theoretical Description. *Journal of the Atmospheric Sciences*, **77**, 3637–3660, https://doi.org/10.1175/JAS-D-19-0243.1.

Moser, D. H., and S. Lasher-Trapp, 2017: The Influence of Successive Thermals on Entrainment and Dilution in a Simulated Cumulus Congestus. *Journal of Atmospheric Sciences*, **74**, 375–392, https://doi.org/10.1175/JAS-D-16-0144.1.

Muller, C. J., and I. M. Held, 2012: Detailed Investigation of the Self-Aggregation of Convection in Cloud-Resolving Simulations. *Journal of the Atmospheric Sciences*, **69**, 2551–2565, https://doi.org/10.1175/JAS-D-11-0257.1.

Naumann, A. K., B. Stevens, C. Hohenegger, and J. P. Mellado, 2017: A Conceptual Model of a Shallow Circulation Induced by Prescribed Low-Level Radiative Cooling. *Journal of the Atmospheric Sciences*, **74**, 3129–3144, https://doi.org/10.1175/JAS-D-17-0030.1.

Nesbitt, S. W., and E. J. Zipser, 2003: The Diurnal Cycle of Rainfall and Convective Intensity according to Three Years of TRMM Measurements. *Journal of Climate*, **16**, 1456–1475, https://doi.org/10.1175/1520-0442(2003)016<1456:TDCORA>2.0.CO;2.

Palm, B. B., and Coauthors, 2021: Spatially Resolved Photochemistry Impacts Emissions Estimates in Fresh Wildfire Plumes. *Geophysical Research Letters*, **48**, e2021GL095443, https://doi.org/10.1029/2021GL095443.

Park, J. M., and S. C. van den Heever, 2021: How does the Environment Modulate Aerosol Impacts on Tropical Sea Breeze Convective Systems? *Atmospheric Chemistry and Physics Discussions*, https://doi.org/10.5194/acp-2021-693.

Park, J. M., S. C. van den Heever, A. L. Igel, L. D. Grant, J. S. Johnson, S. M. Saleeby, S. D. Miller, and J. S. Reid, 2020: Environmental Controls on Tropical Sea Breeze Convection and Resulting Aerosol Redistribution. *Journal of Geophysical Research: Atmospheres*, **125**, e2019JD031699, https://doi.org/10.1029/2019JD031699.

Peters, J. M., 2016: The Impact of Effective Buoyancy and Dynamic Pressure Forcing on Vertical Velocities within Two-Dimensional Updrafts. *Journal of the Atmospheric Sciences*, **73**, 4531–4551, https://doi.org/10.1175/JAS-D-16-0016.1.

——, W. Hannah, and H. Morrison, 2019: The Influence of Vertical Wind Shear on Moist Thermals. *Journal of the Atmospheric Sciences*, **76**, 1645–1659, https://doi.org/10.1175/JAS-D-18-0296.1.

Pierce, A. M., S. M. Loría-Salazar, H. A. Holmes, and M. S. Gustin, 2019: Investigating horizontal and vertical pollution gradients in the atmosphere associated with an urban location in complex terrain, Reno, Nevada, USA. *Atmospheric Environment*, **196**, 103–117, https://doi.org/10.1016/j.atmosenv.2018.09.063.

Posselt, D. J., S. C. van den Heever, and G. L. Stephens, 2008: Trimodal cloudiness and tropical stable layers in simulations of radiative convective equilibrium. *Geophysical Research Letters*, **35**, https://doi.org/10.1029/2007GL033029.

Qian, J.-H., 2008: Why Precipitation Is Mostly Concentrated over Islands in the Maritime Continent. *Journal of the Atmospheric Sciences*, **65**, 1428–1441, https://doi.org/10.1175/2007JAS2422.1.

Ramanathan, V., and Coauthors, 2005: Atmospheric brown clouds: Impacts on South Asian climate and hydrological cycle. *Proc. Natl. Acad. Sci. U.S.A.*, **102**, 5326–5333, https://doi.org/10.1073/pnas.0500656102.

Randall, D. A., and Coauthors, 2019: 100 Years of Earth System Model Development. *Meteorological Monographs*, **59**, 12.1-12.66, https://doi.org/10.1175/AMSMONOGRAPHS-D-18-0018.1.

Redelsperger, J.-L., D. B. Parsons, and F. Guichard, 2002: Recovery Processes and Factors Limiting Cloud-Top Height following the Arrival of a Dry Intrusion Observed during

TOGA COARE. *Journal of the Atmospheric Sciences*, **59**, 2438–2457, https://doi.org/10.1175/1520-0469(2002)059<2438:RPAFLC>2.0.CO;2.

Reid, J. S., and Coauthors, 2019: Observations and hypotheses related to low to middle free tropospheric aerosol, water vapor and altocumulus cloud layers within convective weather regimes: a SEAC⁴RS case study. *Atmos. Chem. Phys.*, **19**, 11413–11442, https://doi.org/10.5194/acp-19-11413-2019.

Riehl, H., and J. S. Malkus, 1958: On the heat balace in the equatorial trough zone. *Geophysica*, **6**, 503–558.

Romps, D. M., and A. B. Charn, 2015: Sticky Thermals: Evidence for a Dominant Balance between Buoyancy and Drag in Cloud Updrafts. *Journal of the Atmospheric Sciences*, **72**, 2890–2901, https://doi.org/10.1175/JAS-D-15-0042.1.

de Roode, S. R. de, A. P. Siebesma, H. J. J. Jonker, and Y. de Voogd, 2012: Parameterization of the Vertical Velocity Equation for Shallow Cumulus Clouds. *Monthly Weather Review*, **140**, 2424–2436, https://doi.org/10.1175/MWR-D-11-00277.1.

de Rooy, W. C., and Coauthors, 2013: Entrainment and detrainment in cumulus convection: an overview. *Quarterly Journal of the Royal Meteorological Society*, **139**, 1–19, https://doi.org/10.1002/qj.1959.

Rougier, J., D. M. H. Sexton, J. M. Murphy, and D. Stainforth, 2009: Analyzing the Climate Sensitivity of the HadSM3 Climate Model Using Ensembles from Different but Related Experiments. *Journal of Climate*, **22**, 3540–3557, https://doi.org/10.1175/2008JCLI2533.1.

Saleeby, S. M., and W. R. Cotton, 2004: A Large-Droplet Mode and Prognostic Number Concentration of Cloud Droplets in the Colorado State University Regional Atmospheric Modeling System (RAMS). Part I: Module Descriptions and Supercell Test Simulations. *Journal of Applied Meteorology and Climatology*, **43**, 182–195, https://doi.org/10.1175/1520-0450(2004)043<0182:ALMAPN>2.0.CO;2.

——, and ——, 2008: A Binned Approach to Cloud-Droplet Riming Implemented in a Bulk Microphysics Model. *Journal of Applied Meteorology and Climatology*, **47**, 694–703.

——, and S. C. van den Heever, 2013: Developments in the CSU-RAMS Aerosol Model: Emissions, Nucleation, Regeneration, Deposition, and Radiation. *Journal of Applied Meteorology and Climatology*, **52**, 2601–2622, https://doi.org/10.1175/JAMC-D-12-0312.1.

Savre, J., 2021: Formation and maintenance of subsiding shells around non-precipitating and precipitating cumulus clouds. *Quarterly Journal of the Royal Meteorological Society*, **147**, 728–745, https://doi.org/10.1002/qj.3942.

Schmeissner, T., R. A. Shaw, J. Ditas, F. Stratmann, M. Wendisch, and H. Siebert, 2015: Turbulent Mixing in Shallow Trade Wind Cumuli: Dependence on Cloud Life Cycle.

Journal of the Atmospheric Sciences, **72**, 1447–1465, https://doi.org/10.1175/JAS-D-14-0230.1.

Scorer, R. S., and F. H. Ludlam, 1953: Bubble theory of penetrative convection. *Quarterly Journal of the Royal Meteorological Society*, **79**, 94–103, https://doi.org/10.1002/qj.49707933908.

Sheffield, A. M., S. M. Saleeby, and S. C. van den Heever, 2015: Aerosol-induced mechanisms for cumulus congestus growth. *Journal of Geophysical Research: Atmospheres*, **120**, 8941–8952, https://doi.org/10.1002/2015JD023743.

Sherwood, S. C., D. Hernández-Deckers, M. Colin, and F. Robinson, 2013: Slippery Thermals and the Cumulus Entrainment Paradox. *Journal of the Atmospheric Sciences*, **70**, 2426–2442, https://doi.org/10.1175/JAS-D-12-0220.1.

Siebesma, A. P., 1998: Shallow Cumulus Convection. *Buoyant Convection in Geophysical Flows*, E.J. Plate, E.E. Fedorovich, D.X. Viegas, and J.C. Wyngaard, Eds., *NATO ASI Series*, Springer Netherlands, 441–486.

Smalley, K. M., and A. D. Rapp, 2020: The Role of Cloud Size and Environmental Moisture in Shallow Cumulus Precipitation. *Journal of Applied Meteorology and Climatology*, **59**, 535–550, https://doi.org/10.1175/JAMC-D-19-0145.1.

Stevens, B., 2007: On the Growth of Layers of Nonprecipitating Cumulus Convection. *Journal of the Atmospheric Sciences*, **64**, 2916–2931, https://doi.org/10.1175/JAS3983.1.

Takayabu, Y. N., S. Shige, W.-K. Tao, and N. Hirota, 2010: Shallow and Deep Latent Heating Modes over Tropical Oceans Observed with TRMM PR Spectral Latent Heating Data. *Journal of Climate*, **23**, 2030–2046, https://doi.org/10.1175/2009JCLI3110.1.

Takemi, T., O. Hirayama, and C. Liu, 2004: Factors responsible for the vertical development of tropical oceanic cumulus convection. *Geophysical Research Letters*, **31**, https://doi.org/10.1029/2004GL020225.

Tao, W.-K., J.-P. Chen, Z. Li, C. Wang, and C. Zhang, 2012: Impact of aerosols on convective clouds and precipitation. *Reviews of Geophysics*, **50**, https://doi.org/10.1029/2011RG000369.

Tian, Y., Z. Kuang, M. S. Singh, and J. Nie, 2019: The Vertical Momentum Budget of Shallow Cumulus Convection: Insights From a Lagrangian Perspective. *Journal of Advances in Modeling Earth Systems*, **11**, 113–126, https://doi.org/10.1029/2018MS001451.

——, Y. Zhang, S. A. Klein, and C. Schumacher, 2021: Interpreting the Diurnal Cycle of Clouds and Precipitation in the ARM GoAmazon Observations: Shallow to Deep Convection Transition. *Journal of Geophysical Research: Atmospheres*, **126**, e2020JD033766, https://doi.org/10.1029/2020JD033766.

Twomey, S., 1977: The Influence of Pollution on the Shortwave Albedo of Clouds. *Journal of the Atmospheric Sciences*, **34**, 1149–1152, https://doi.org/10.1175/1520-0469(1977)034<1149:TIOPOT>2.0.CO;2.

Verheggen, B., and Coauthors, 2007: Aerosol partitioning between the interstitial and the condensed phase in mixed-phase clouds. *Journal of Geophysical Research: Atmospheres*, **112**, https://doi.org/10.1029/2007JD008714.

Waite, M. L., and B. Khouider, 2010: The Deepening of Tropical Convection by Congestus Preconditioning. *Journal of Atmospheric Sciences*, **67**, 2601–2615, https://doi.org/10.1175/2010JAS3357.1.

Walko, R. L., and Coauthors, 2000: Coupled Atmosphere–Biophysics–Hydrology Models for Environmental Modeling. *Journal of Applied Meteorology and Climatology*, **39**, 931–944, https://doi.org/10.1175/1520-0450(2000)039<0931:CABHMF>2.0.CO;2.

Wang, C., D. Kim, A. M. L. Ekman, M. C. Barth, and P. J. Rasch, 2009: Impact of anthropogenic aerosols on Indian summer monsoon. *Geophysical Research Letters*, **36**, https://doi.org/10.1029/2009GL040114.

Wang, X., and M. Zhang, 2014: Vertical velocity in shallow convection for different plume types. *Journal of Advances in Modeling Earth Systems*, **6**, 478–489, https://doi.org/10.1002/2014MS000318.

Wang, Y., J. Wang, R. C. Levy, Y. R. Shi, S. Mattoo, and J. S. Reid, 2021: First Retrieval of AOD at Fine Resolution Over Shallow and Turbid Coastal Waters From MODIS. *Geophysical Research Letters*, **48**, e2021GL094344, https://doi.org/10.1029/2021GL094344.

Wei, J., L. Sun, Y. Peng, L. Wang, Z. Zhang, M. Bilal, and Y. Ma, 2018: An Improved High-Spatial-Resolution Aerosol Retrieval Algorithm for MODIS Images Over Land. *Journal of Geophysical Research: Atmospheres*, **123**, 12,291-12,307, https://doi.org/10.1029/2017JD027795.

Yang, G.-Y., and J. Slingo, 2001: The Diurnal Cycle in the Tropics. *Monthly Weather Review*, **129**, 784–801, https://doi.org/10.1175/1520-0493(2001)129<0784:TDCITT>2.0.CO;2.

Zipser, E. J., 2003: Some Views On "Hot Towers" after 50 Years of Tropical Field Programs and Two Years of TRMM Data. *Cloud Systems, Hurricanes, and the Tropical Rainfall Measuring Mission (TRMM): A Tribute to Dr. Joanne Simpson*, W.-K. Tao and R. Adler, Eds., *Meteorological Monographs*, American Meteorological Society, 49–58.

APPENDIX: DERIVATION OF THE COMPRESSIBLE VERTICAL MOMENTUM BUDGET FOR A CLOUD ENSEMBLE

First, the continuity equation can be written in flux form as:

$$\frac{\partial \rho}{\partial t} + \vec{\nabla} \cdot (\rho \vec{v}) = 0 \tag{1}$$

where ρ is the density and $\vec{v}$ is the full velocity vector.

Given this, we can define some area of interest c (e.g. congestus updrafts) denoted by an activation function $I(x, y, z, t)$ that is equal to 1 for the region of interest and 0 otherwise. The conditional mean of some field ψ taken only over the area of interest is: $[\psi]^c = \frac{1}{A_c} \int_c \psi dA = \frac{1}{A_c} \int_{domain} \psi I dA$, where A_c is the area of interest. By Leibniz's Rule, conditional averages of derivatives include an extra term as described in Siebesma et al. (1998): $\left[\frac{\partial \psi}{\partial z}\right]^c = \frac{1}{A_c} \int_c \frac{\partial \psi}{\partial z} dA = \frac{1}{A_c} \frac{\partial A_c [\psi]^c}{\partial z}$. We ignore the boundary terms in Leibniz's Rule by defining the conditional area as updrafts such that ψ is constant along the boundaries.

We can then take the conditional average of equation (1) to be:

$$\frac{1}{A_c} \frac{\partial A_c [\rho]^c}{\partial t} = -\left[\vec{\nabla}_H \cdot (\rho \overrightarrow{v_H})\right]^c - \frac{1}{A_c} \frac{\partial A_c [\rho w]^c}{\partial z} \tag{2}$$

For convenience, we define $\rho_c = \frac{\int_{domain} I \rho dA}{A_c}$ to be the conditional average of ρ , and $w_c = \frac{\int_{domain} I \rho w dA}{\int_{domain} I \rho dA} = \frac{[\rho w]^c}{\rho_c}$ to be the density-weighted conditional average of the vertical velocity w.

Substituting this and using Green's theorem to simplify the divergence term into a closed integral over the conditionally-selected area c makes equation (2) equivalent to:

$$\frac{1}{A_c}\frac{\partial A_c \rho_c}{\partial t} = -\frac{1}{A_c}\oint \overrightarrow{v_H}\cdot \hat{n}\rho dC - \frac{1}{A_c}\frac{\partial A_c \rho_c w_c}{\partial z} \tag{3}$$

Similarly, the momentum equation can be written as:

$$\frac{Dw}{Dt} = \frac{\partial w}{\partial t} + \vec{v}\cdot\vec{\nabla}w = -\frac{1}{\rho}\frac{\partial p'}{\partial z} + B \tag{4}$$

where p' is the perturbation from base state pressure and B is buoyancy.

Combining equation (4) times ρ with equation (1) times w gives:

$$\frac{\partial \rho w}{\partial t} + \vec{\nabla}\cdot(\rho w\vec{v}) = -\frac{\rho}{\rho}\frac{\partial p'}{\partial z} + \rho B \tag{5}$$

This can be conditionally sampled as above

$$\frac{1}{A_c}\frac{\partial A_c[\rho w]^c}{\partial t} = -\frac{1}{A_c}\oint \overrightarrow{v_H}\cdot \hat{n}\rho w dC - \frac{1}{A_c}\frac{\partial A_c[\rho w^2]^c}{\partial z} - \left[\frac{\partial p'}{\partial z}\right]^c + [\rho B]^c \tag{6}$$

$$= \frac{1}{A_c}\frac{\partial A_c \rho_c w_c}{\partial t} = \frac{w_c}{A_c}\frac{\partial A_c \rho_c}{\partial t} + \rho_c \frac{\partial w_c}{\partial t}$$

Where the term $w = w_c + w'$ can be decomposed such that w' is the perturbation from the ensemble value of w_c. Thus, we obtain:

$$[\rho w^2]^c = \frac{\int_{domain} I\rho w^2 dA}{A_c} = \frac{\int_{domain} I\rho(w_c + w')^2 dA}{A_c}$$

$$= \frac{\int_{domain} I\rho w_c^2 dA}{A_c} + \frac{\int_{domain} I\rho w'^2 dA}{A_c}$$

$$= w_c^2 \frac{\int_{domain} I\rho dA}{A_c} + \frac{\int_{domain} I\rho w'^2 dA}{A_c} = p_c w_c^2 + \left[\rho w'^2\right]^c \tag{7}$$

Substituting this into equation (6) gives:

$$\frac{w_c}{A_c}\frac{\partial A_c \rho_c}{\partial t} + \rho_c \frac{\partial w_c}{\partial t}$$

$$= -\frac{1}{A_c}\oint \overrightarrow{v_H}\cdot \hat{n}\rho w dC - \frac{1}{A_c}\frac{\partial A_c p_c w_c^2}{\partial z} - \frac{1}{A_c}\frac{\partial A_c[\rho w'^2]^c}{\partial z} - \left[\frac{\partial p'}{\partial z}\right]^c + [\rho B]^c$$

$$\frac{w_c}{A_c}\frac{\partial A_c\rho_c}{\partial t}+\rho_c\frac{\partial w_c}{\partial t}$$

$$=-\frac{1}{A_c}\oint\overrightarrow{v_H}\cdot\hat{n}\rho w dC-\frac{w_c^2}{A_c}\frac{\partial A_c p_c}{\partial z}-\rho_c\frac{\partial w_c^2}{\partial z}\qquad-\frac{1}{A_c}\frac{\partial A_c\left[\rho w'^2\right]^c}{\partial z}\ -\left[\frac{\partial p'}{\partial z}\right]^c$$

$$+[\rho B]^c \qquad (8)$$

The continuity equation in (3) can be substituted into the left-hand side:

$$\frac{w_c}{A_c}\left(-\oint\overrightarrow{v_H}\cdot\hat{n}\rho dC-\frac{\partial A_c\rho_c w_c}{\partial z}\right)+\rho_c\frac{\partial w_c}{\partial t}$$

$$=-\frac{1}{A_c}\oint\overrightarrow{v_H}\cdot\hat{n}\rho w dC-\frac{w_c^2}{A_c}\frac{\partial A_c p_c}{\partial z}-\rho_c\frac{\partial w_c^2}{\partial z}-\frac{1}{A_c}\frac{\partial A_c\left[\rho w'^2\right]^c}{\partial z}\ -\left[\frac{\partial p'}{\partial z}\right]^c$$

$$+[\rho B]^c$$

$$\rho_c\frac{\partial w_c}{\partial t}=-\frac{1}{A_c}\oint\overrightarrow{v_H}\cdot\hat{n}\rho(w-w_c)dC+\frac{w_c}{A_c}\frac{\partial\rho_c w_c A_c}{\partial z}-\frac{w_c^2}{A_c}\frac{\partial A_c p_c}{\partial z}-\rho_c\frac{\partial w_c^2}{\partial z}$$

$$-\frac{1}{A_c}\frac{\partial A_c\left[\rho w'^2\right]^c}{\partial z}\ -\left[\frac{\partial p'}{\partial z}\right]^c+[\rho B]^c$$

$$=-\frac{1}{A_c}\oint\overrightarrow{v_H}\cdot\hat{n}\rho(w-w_c)dC+\frac{w_c^2}{A_c}\frac{\partial\rho_c A_c}{\partial z}-\frac{w_c^2}{A_c}\frac{\partial A_c p_c}{\partial z}-\frac{\rho_c}{2}\frac{\partial w_c^2}{\partial z}$$

$$-\frac{1}{A_c}\frac{\partial A_c\left[\rho w'^2\right]^c}{\partial z}\ -\left[\frac{\partial p'}{\partial z}\right]^c+[\rho B]^c$$

$$\rho_c\frac{\partial w_c}{\partial t}=-\frac{1}{A_c}\oint\overrightarrow{v_H}\cdot\hat{n}\rho(w-w_c)dC-\frac{\rho_c}{2}\frac{\partial w_c^2}{\partial z}-\frac{1}{A_c}\frac{\partial A_c\left[\rho w'^2\right]^c}{\partial z}\ -\left[\frac{\partial p'}{\partial z}\right]^c+[\rho B]^c \quad (9)$$

Finally, we define a density-weighted buoyancy $B_c=\frac{\int_{domain}I\rho B dA}{\int_{domain}I\rho dA}=\frac{[\rho B]^c}{\rho_c}$. Dividing equation (9) by ρ_c gives the following equation for the conditionally-sampled vertical momentum budget:

$$\underbrace{\frac{\partial w_c}{\partial t}}_{time\ tendency} = \underbrace{B_c}_{(1)\ buoyancy} + \underbrace{-\frac{1}{\lfloor\rho\rfloor_c}\left[\frac{\partial p'}{\partial z}\right]_c}_{(2)\ perturbation\ pressure\ gradient}$$

$$+ \underbrace{-\frac{1}{A_c\lfloor\rho\rfloor_c}\oint_c \overrightarrow{v_H}\cdot\hat{n}(w-w_c)\rho dC}_{(3)\ momentum\ entrainment} + \underbrace{-\frac{1}{2}\frac{\partial {w_c}^2}{\partial z}}_{(4)\ vertical\ advection}$$

$$+ \underbrace{-\frac{1}{A_c\lfloor\rho\rfloor_c}\frac{\partial A\lfloor\rho(w-w_c)\rfloor_c^{\,2}}{\partial z}}_{(5)\ turbulent\ vertical\ flux} \qquad (10)$$